

# **Modelling of a Thermally Insulated Solar Hydrogen System: Utilizing the Operational Heat**

*Submitted in partial fulfilment of the requirements for the degree of*  
***B.Tech – M.Tech (Dual Degree)***



**EN 594: Dual Degree Project II**

By

**Atmuri Mahesh Sreshti**

(Roll no. 18D170009)

Under the guidance of

**Prof. Prakash Chandra Ghosh**

Department of Energy Science and Engineering

Indian Institute of Technology Bombay

Mumbai 400076

June 2023



## Acceptance Certificate

The report entitled “**Modelling of a Thermally Insulated Solar Hydrogen System: Utilizing the Operational Heat**” submitted by **Atmuri Mahesh Sreshti** (Roll No. 18D170009) may be accepted for being evaluated.

Guide: Prof. Prakash C. Ghosh

Date:

Place:



## Declaration

This statement serves as a formal declaration affirming the originality and integrity of the ideas presented in this submission. The content within this report has been meticulously composed using my own words. In instances where concepts or textual excerpts from external sources have been incorporated, diligent effort has been made to appropriately cite and reference these original works. I acknowledge that all sources referenced in the production of this report have been duly and accurately acknowledged, ensuring that proper credit is given to the respective authors or creators. I further acknowledge and uphold the principles of academic honesty and integrity, vowing to refrain from any form of misrepresentation, fabrication, or falsification of information, whether it pertains to ideas, data, facts, or sources contained within this submission. It is crucial to emphasize that any violation of these ethical principles may result in disciplinary measures enforced by the institution. Additionally, legal consequences may ensue if proper citation or permissions were not obtained from the relevant sources when required. By making this declaration, I affirm my commitment to the highest standards of academic integrity and the responsible and conscientious creation of this report.

Date: June 28, 2023

Atmuri Mahesh Sreshti (18D170009)



## Acknowledgement

I would like to extend my sincere and immense gratitude to my guide, Prof. Prakash C. Ghosh, Department of Energy Science and Engineering, Indian Institute of Technology Bombay, for his guidance and encouragement. I would also like to thank our Faculty Advisor, Prof. Balasubramaniam Kavaipatti for his support and coordination.

I sincerely thank the Ph.D. scholars of the Fuel Cell Laboratory, Department of Energy Science and Engineering, who provided constant support and guidance to me in multiple aspects. I would like to thank my friends who were there to brainstorm ideas and debug many problems during my research. I would like to acknowledge and thank my family for being the source of my inspiration.

Lastly, I would like to thank IIT Bombay for this opportunity of conducting extensive research work via this Dual Degree Project which enabled me to interact with inspiring individuals, and acquire new skills and knowledge.

Atmuri Mahesh Sreshti

## Abstract

This report presents a comprehensive investigation into the performance of a solar-powered hydrogen generation and storage system under various load scenarios. The system integrates a solar photovoltaic (PV) array, electrolyzer, fuel cell, and hydrogen storage to harness solar energy for the production and utilization of hydrogen. Through modelling and simulation, the operational characteristics and efficiencies of each component are analyzed to optimize energy utilization and system performance.

The study begins by providing an in-depth explanation of the science behind a solar hydrogen system, highlighting the interactions and functions of the individual components. The results demonstrate the efficient conversion of solar energy by the PV array, facilitating consistent hydrogen production by the electrolyzer. The fuel cell effectively utilizes the generated hydrogen and oxygen to produce power. Analysis of the system's performance under different load scenarios reveals its adaptability and responsiveness, with positive net hydrogen volume observed in all cases.

The importance of load management and system design optimization is emphasized as key factors in maximizing energy utilization and overall system efficiency. Evaluation of the efficiencies of the solar PV array, electrolyzer, and fuel cell provides valuable insights for system enhancements and performance optimization. The findings contribute to the advancement of sustainable energy solutions by promoting the effective utilization of renewable resources and emphasizing the importance of efficient energy management.

This study serves as a valuable resource for researchers and engineers involved in the design and optimization of solar-powered hydrogen generation and storage systems. The results highlight the system's capabilities, providing guidance for further improvements and practical implementation. By harnessing solar energy and efficiently converting it into hydrogen, this system showcases the potential for sustainable and clean energy solutions in a variety of applications.

**Keywords:** Solar hydrogen system, solar PV, electrolyzer, fuel cell, hydrogen storage tank, thermally insulated system, load modelling, Simulink modelling, energy efficiency.





# Table of Contents

Acceptance Certificate .....	ii
Declaration .....	iii
Acknowledgement .....	iv
List of Tables .....	ix
List of Figures .....	x
Nomenclature .....	xiii
1. Introduction.....	1
2. Solar Hydrogen System .....	2
2.1 Types of Solar Hydrogen Systems.....	2
2.1.1 Photocatalytic.....	2
2.1.2 Photoelectrochemical .....	3
2.1.3 Photobiological .....	3
2.1.4 Solar Thermal.....	3
2.2 Types of Photoelectrochemical (PEC) Solar Hydrogen Systems .....	4
2.2.1 Fully Integrated/Wireless.....	4
2.2.2 Partially Integrated/Wired.....	4
2.2.3 Non-Integrated/Modular .....	4
2.3 Solar Hydrogen Systems Examples .....	5
3. System Design and Selection of Components .....	7
3.1 System Design for Simulation .....	7
3.2 Solar PV Selection .....	8
3.3 Electrolyzer Selection .....	9
3.4 Fuel Cell Selection.....	10
3.5 Passive Solar Tent Design .....	11
3.5.1 South-Facing Wall Design.....	11
3.5.2 Internal Design.....	12
4. Modelling of Solar Hydrogen System .....	14
4.1 Solar PV Modelling .....	14
4.2 Electrolyzer Modelling .....	17
4.2.1 Anode.....	18
4.2.2 Cathode .....	19
4.2.3 Membrane .....	20
4.2.4 Voltage.....	23



4.3 Hydrogen Storage Modelling.....	26
4.4 Fuel Cell Modelling .....	26
4.4.1 Anode H <sub>2</sub> Flow.....	27
4.4.2 Cathode O <sub>2</sub> Flow .....	28
4.4.3 Fuel Cell.....	29
4.5 Passive Solar Tent Modelling .....	31
4.5.1 Net Load Coefficient.....	32
4.5.2 Degree Days.....	32
4.5.3 Solar Savings Fraction .....	32
4.5.4 Auxiliary Heat.....	33
4.6 Overall System Model .....	33
5. Results and Discussion .....	36
5.1 Passive Solar Tent.....	36
5.2 Solar PV .....	36
5.3 Electrolyzer .....	38
5.4 Fuel Cell.....	40
5.5 Overall Model .....	41
5.5.1 Variable Load.....	43
5.5.2 No Load .....	47
5.5.3 Constant Load .....	49
5.5.4 Comparison .....	51
6. Conclusion .....	55
References.....	56





## List of Tables

2.1	Examples of solar hydrogen systems.....	6
3.1	Vikram Solar Eldora polycrystalline Si PV modules.....	8
3.2	Vikram Solar Somera monocrystalline Si PERC PV modules.....	9
4.1	Technical specifications of Polycab solar module.....	17
4.2	Parameters used in the electrolyzer model.....	24
4.3	Parameters used in the fuel cell model.....	30



## List of Figures

2.1	Single semiconductor: Mechanism of photocatalytic water splitting.....	2
2.2	Fully integrated device.....	3
2.3	Partially integrated device.....	3
2.4	Non-integrated device.....	3
2.5	Fully integrated system.....	4
2.6	Cross-sectional view of a PV water-splitting device.....	4
2.7	Cross-sectional view of PEM, alkaline electrolysis cells.....	5
2.8	Cross-sectional view of flow-by, flow- through electrodes.....	5
3.1	Flowchart of thermally insulated solar hydrogen system.....	7
3.2	Monocrystalline, polycrystalline, and thin film solar modules.....	8
3.3	General depiction of an alkaline electrolyser.....	9
3.4	General depiction of a PEM electrolyser.....	10
3.5	General depiction of a solid oxide electrolyser.....	10
3.6	Direct gain system.....	12
3.7	Indirect gain system.....	12
3.8	Design of the solar tent.....	12
4.1	Representative circuit diagram for a solar cell.....	14
4.2	Simulink model of the solar module.....	17
4.3	Simulink model of the electrolyzer.....	18
4.4	Simulink model of the anode subsystem in the electrolyzer.....	19
4.5	Simulink model of the cathode subsystem in the electrolyzer .....	20
4.6	Simulink model of the membrane subsystem in the electrolyzer .....	22
4.7	Simulink model of the effective diffusion subsystem in the electrolyzer .....	23
4.8	Simulink model of the voltage subsystem in the electrolyzer .....	25
4.9	Simulink model of the hydrogen storage tank.....	26
4.10	Simulink model of the fuel cell.....	27
4.11	Simulink model of anode H <sub>2</sub> flow subsystem in the fuel cell .....	28
4.12	Simulink model of the cathode O <sub>2</sub> flow subsystem in the fuel cell .....	28

4.13	Simulink model of the fuel cell subsystem in the fuel cell .....	31
4.14	Flowchart of calculations to estimate auxiliary heating requirement.....	31
4.15	Calculation of Degree Days for Leh.....	32
4.16	Simulink model of entire solar hydrogen system.....	35
5.1	Dimensions of the passive solar tent.....	36
5.2	IV curve of solar model under STC.....	37
5.3	IV curve of solar model under variable irradiance.....	37
5.4	Variation of output power with irradiance at constant temperature.....	38
5.5	Polarization curve of electrolyzer.....	39
5.6	Contribution of different overpotentials to the operating voltage of electrolyzer.....	39
5.7	Polarization curve of fuel cell.....	40
5.8	Contribution of different overpotentials to the operating voltage of fuel cell.....	41
5.9	Daily irradiance variation in Leh on 21 June.....	42
5.10	Daily temperature variation in Leh on 21 June.....	42
5.11	Power output of solar PV array.....	43
5.12	Daily load profile for variable load.....	43
5.13	Gas molar flow rate output of electrolyzer under variable load conditions.....	44
5.14	Power output of fuel cell under variable load conditions.....	45
5.15	Net volume of hydrogen in hydrogen storage under variable load conditions.....	45
5.16	Variation of device efficiencies under variable load conditions.....	46
5.17	Operational heat produced by electrolyzer & fuel cell under variable load conditions..	47
5.18	Gas molar flow rate output of electrolyzer under no load conditions.....	47
5.19	Net volume of hydrogen in hydrogen storage under no load conditions.....	48
5.20	Variation of device efficiencies under no load conditions.....	48
5.21	Operational heat produced by electrolyzer under no load conditions.....	49
5.22	Gas molar flow rate output of electrolyzer under constant load conditions.....	49
5.23	Power output of fuel cell under constant load conditions.....	50
5.24	Net volume of hydrogen in hydrogen storage tank under constant load conditions.....	50
5.25	Variation of device efficiencies under constant load conditions.....	51
5.26	Operational heat produced by electrolyzer & fuel cell under constant load conditions.	51



- 5.27 Comparison of gas molar flow rate output of electrolyzer under different loads.....52
- 5.28 Comparison of net volume of hydrogen in hydrogen storage under different loads.....53



## Nomenclature

<i>BOP</i>	Balance Of Plant
<i>CH<sub>3</sub>OH</i>	Methanol
<i>CO</i>	Carbon Monoxide
<i>CO<sub>2</sub></i>	Carbon Dioxide
<i>DC</i>	Direct Current
<i>DD</i>	Degree Day
<i>GaAs</i>	Gallium Arsenide
<i>H<sub>2</sub></i>	Hydrogen
<i>H<sub>2</sub>O</i>	Water
<i>HER</i>	Hydrogen Evolution Reaction
<i>HHV</i>	Higher Heating Value
<i>I<sub>mp</sub></i>	Current at maximum power
<i>I<sub>sc</sub></i>	Short circuit current
<i>K<sub>2</sub>CO<sub>3</sub></i>	Potassium Carbonate
<i>KOH</i>	Potassium Hydroxide
<i>Li<sub>2</sub>CO<sub>3</sub></i>	Lithium Carbonate
<i>MPPT</i>	Maximum Power Point Tracking
<i>NaOH</i>	Sodium Hydroxide
<i>NLC</i>	Net Load Coefficient
<i>NOCT</i>	Nominal Operating Cell Temperature
<i>NREL</i>	National Renewable Energy Laboratory
<i>NSRDB</i>	National Solar Radiation Database
<i>O<sub>2</sub></i>	Oxygen
<i>OER</i>	Oxygen Evolution Reaction



$PEC$	Photoelectrochemical
$PEM$	Polymer Electrolyte Membrane / Proton Exchange Membrane
$PEMFC$	Polymer Electrolyte Membrane Fuel Cell
$PERC$	Passivated Emitter and Rear Contact
$P_{max}$	Maximum Power
$PV$	Photovoltaic
$Q_{aux}$	Auxiliary Heat
$Si$	Silicon
$SOEC$	Solid Oxide Electrolyzer Cell
$SOFC$	Solid Oxide Fuel Cell
$SSF$	Solar Saving Fraction
$STH$	Solar-To-Hydrogen
$T_{amb}$	Ambient Temperature
$V_{mp}$	Voltage at maximum power
$V_{oc}$	Open circuit voltage
$\Delta G^o$	Standard Gibbs Free Energy
$\eta$	Efficiency



# 1. Introduction

The increasing demand for clean and sustainable energy sources has driven significant research and development in renewable energy technologies. Solar energy, in particular, has emerged as a promising solution due to its abundant availability and environmental benefits. However, the intermittent nature of solar power generation poses challenges for its efficient utilization and integration into the existing energy infrastructure.

To overcome this challenge, energy storage technologies, such as hydrogen generation and storage systems, have gained attention. Hydrogen, a versatile energy carrier, can be produced through electrolysis using electricity generated from solar photovoltaic (PV) arrays. The generated hydrogen can then be stored and utilized later in fuel cells to produce electricity on demand. This integrated solar-powered hydrogen system presents a viable solution for addressing the intermittency issue and achieving a sustainable energy supply. Hence combining solar energy with hydrogen production can lead to carbon-free fuel, at least during operation.

In high altitude and strategic locations, supplying and replenishing essential resources for the military becomes an arduous and expensive task. The low oxygen levels and challenging energy supply further exacerbate the difficulties faced in these environments. Moreover, the extreme sub-zero temperatures make nighttime conditions harsh and demanding. Therefore, there is a critical requirement for the armed forces to have access to electricity, fuel (hydrogen), oxygen, and heat in such regions. This is where solar hydrogen technology can play a crucial role in bridging the gap between these essential necessities and effective actions.

The objective of this project is to design and model a multifunctional thermally insulated solar hydrogen system that addresses the diverse needs of high-altitude applications. This system will serve as a versatile solution, capable of generating electricity for general usage and electrolysis, producing hydrogen and oxygen, and providing thermal warmth within the vessel. As the electrolyzer and fuel cell operations result in heat evolution due to their inefficiencies, the excess heat will be harnessed and effectively utilized to maintain temperature levels using advanced thermal insulation technology. The developed system holds potential for deployment by both the armed forces and local communities residing in high altitude regions.

By leveraging solar energy and harnessing its power to produce hydrogen, oxygen, electricity, and heat, this innovative system aims to overcome the logistical and operational challenges faced in remote and hostile environments. The integration of various functionalities within a single unit enables efficient resource utilization, reducing the dependence on external supply chains and minimizing the associated costs. Additionally, the thermal insulation technology implemented in the system ensures optimal temperature maintenance, enhancing comfort and survivability for personnel operating in extreme conditions.

Through the successful implementation of this multifunctional solar hydrogen system, significant advancements can be made in supporting military operations and improving the quality of life for individuals residing in high altitude areas. The following sections of this report will delve into the technical details, modelling results, and performance analysis of the system, providing valuable insights and recommendations for further development and deployment in real-world scenarios.



## 2. Solar Hydrogen System

Hydrogen can be produced by different methods, including natural gas reforming/gasification, electrolysis, and fermentation. Unlike other methods, electrolysis can potentially convert water to hydrogen without any carbon emissions. This is possible provided the electricity is from a renewable source or non-carbon-emitting fuel. Splitting of water into hydrogen and oxygen is an endothermic reaction, i.e., it requires energy to complete the reaction. Production of one mole of hydrogen requires 237 kJ of free energy under standard conditions. [4]



There are multiple renewable sources which can be coupled with electrolysis to produce “green hydrogen.” This study focuses on solar energy as the renewable source as it is abundant and immensely available worldwide. It is an appealing method of storing chemical energy and providing “green hydrogen” to the industry. Using such a storage system also helps solve some of the challenges associated with the intermittency of solar energy, unfavourable sunshine conditions, and seasonal storage.

Over the last few decades, intensive research led to a significant improvement in the solar-to-hydrogen (STH) efficiencies and stability of the solar water splitting devices. Nevertheless, this method did not reach the competitive levels yet with other large-scale hydrogen production technologies that produce in excess of 50 million t/yr from non-renewables worldwide. Current researchers focus on increasing the lifetime, improving efficiency/performance, and, most importantly, reducing the cost of eventual large-scale implementation. [1]

### 2.1 Types of Solar Hydrogen Systems

There are mainly 4 types of solar hydrogen systems: photocatalytic, photoelectrochemical, photobiological, and solar thermal.

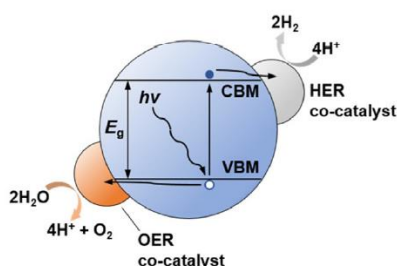


Figure 2.1 Single semiconductor: Mechanism of photocatalytic water splitting [2]

#### 2.1.1 Photocatalytic

When a photon of energy higher than the bandgap of semiconductor is incident, an electron is excited from its valence band to the conduction band leaving behind a hole. For the hydrogen evolution reaction (HER) and oxygen evolution reaction (OER) to begin, these electrons and holes must be separated and diffused to the semiconductor's exterior. [2]

### 2.1.2 Photoelectrochemical

There are three methods by which PEC devices convert solar irradiance to hydrogen: fully integrated / wireless, partially integrated / wired, non-integrated / modular. In the first type, the fully integrated / wireless devices, the solar module and the electrocatalysts are in direct touch. In the partially integrated / wired photoelectrochemical devices, one of the oxidation side or reduction side catalyst is in direct contact with the solar module, while the catalyst on the other electrode is externally connected via electrical wires. Both fully integrated and partially integrated devices convert sunlight to hydrogen via electrolysis in a single device. [1]

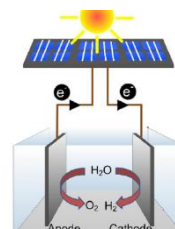
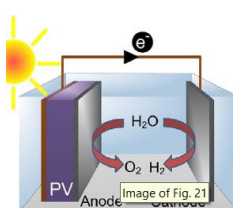
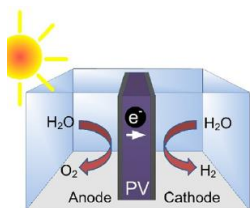


Figure 2.2 Fully integrated device    Figure 2.3 Partially integrated device    Figure 2.4 Non-integrated device [2]

The third type of devices, the non-integrated devices also called modular devices comprise of 2 discrete components: PV cells and electrolyzer. These two components are connected externally via electrical wiring to produce hydrogen. [2]

### 2.1.3 Photobiological

Photobiological hydrogen production has received greater attention in the past two decades as an upcoming technology for industry scale  $H_2$  production owing to its effectively negative carbon footprint and harmless biochemical reaction conditions. Microalgae, purple non-sulfur bacteria (PNSB), and cyanobacteria have shown photobiological hydrogen evolution through different mechanisms. [2]

Cyanobacteria and microalgae exhibit an activity that syncs with the irradiance-reliant levels of photosynthesis called direct biophotolysis of water. Guided by photocatalytic reactions, electrons are first removed from  $H_2O$  & then transported to redox intermediary ferredoxin. Hydrogenases extracts electrons from the reduced ferredoxin in place of embedding carbon dioxide through the irradiance-unrestrained reactions of photosynthesis. This catalyses the HER utilizing the protons extracted from water. [2]

### 2.1.4 Solar Thermal

Concentrated solar energy is utilised to achieve higher temperatures in a reaction chamber to steer the electrolysis process. This phenomenon is also known as solar thermal water splitting, another method towards the production of “green hydrogen.” Solar collectors and receivers of different concentration factors, dimensions, and power capacities have been developed over the years for various solar thermal applications worldwide. Some of them include concentrating collector, flat plate collector, parabolic collector, and vacuum tube collector. Hence it is practical to integrate a thermochemical water splitting device with an existing solar thermal power plant/device matching their power capacities. [3]

## 2.2 Types of Photoelectrochemical (PEC) Solar Hydrogen Systems

Photoelectrochemical water splitting devices are classified into three categories depending on how the electrolysis device and light absorber are connected/integrated. They are fully integrated / wireless, partially integrated / wired, non-integrated / modular.

### 2.2.1 Fully Integrated/Wireless

Attempts to make a fully integrated device started in 1990s. OER and HER catalysts were sputtered into amorphous silicon solar cells (triple junction) ( $0.27 \text{ cm}^2$  active area). Perovskites were also tried as light absorbers for these devices but failed due to their vulnerability on exposure to moisture. Although the fully integrated devices are more economically viable than wired versions, they are lesser efficient. They need to be encapsulated to prevent damage of the solar cells. Also, any disturbances in the liquid electrolyte might cause optical disturbances in the form of bubbles reducing their STH efficiencies. [2]

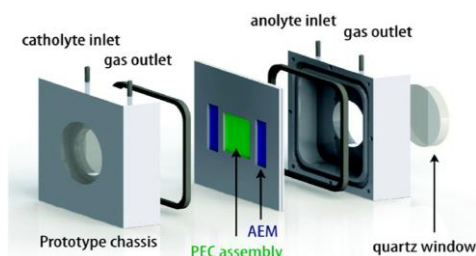


Figure 2.5 Fully integrated system [2]

### 2.2.2 Partially Integrated/Wired

A highly publicised partially integrated device had a p-type  $\text{GaInP}_2$  photocathode coupled with a GaAs p-n junction. The solar to hydrogen efficiency of this device was reported as 12.4%. There were many more demonstrations of different silicon based solar cells as the light absorber with higher active areas but with lower STH efficiency due to the problems of scaling up the devices. Researchers came up with photoelectrodes composed of abundantly available earth materials. [2]

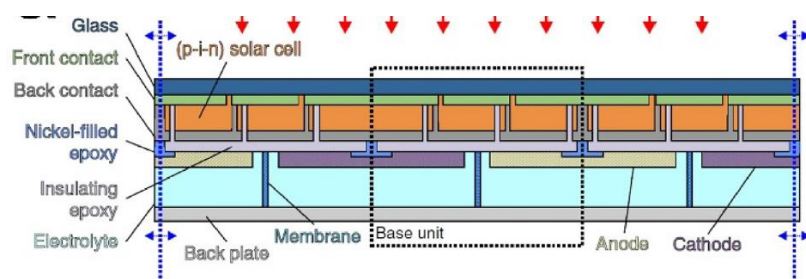


Figure 2.6 Cross-sectional view of a PV water-splitting device [4]

### 2.2.3 Non-Integrated/Modular

For scaling up solar hydrogen production at an industrial scale, modular devices seem to be the best bet going forward as they are very simple in comparison to other integrated devices. They are just a combination of common photovoltaic modules and electrolyzers.

Modular devices can be of two types: membrane-based and membraneless electrolyzer-based system. Within membrane-based devices, there are alkaline electrolyzers and polymer electrolyte membrane electrolyzers (PEM).

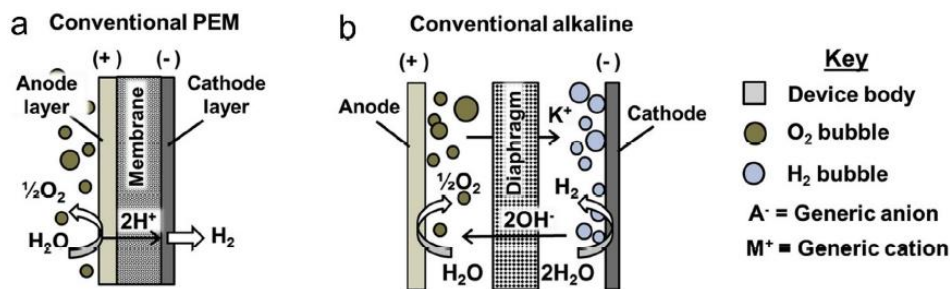


Figure 2.7 Cross-sectional view of PEM, alkaline electrolysis cells [2]

In membraneless devices, there are two types of devices: flow-by electrodes (Type I) and flow-through electrodes (Type II). In flow-by electrodes, H<sub>2</sub> and O<sub>2</sub> which are flowing along the electrode surfaces are carried by aqueous electrolyte. They are separated in the downstream area with H<sub>2</sub> and O<sub>2</sub> rich electrolytes. In flow-through electrodes, the electrolyte flows through the electrode crevice in the metallic mesh. This carries the products into respective channels. [2]

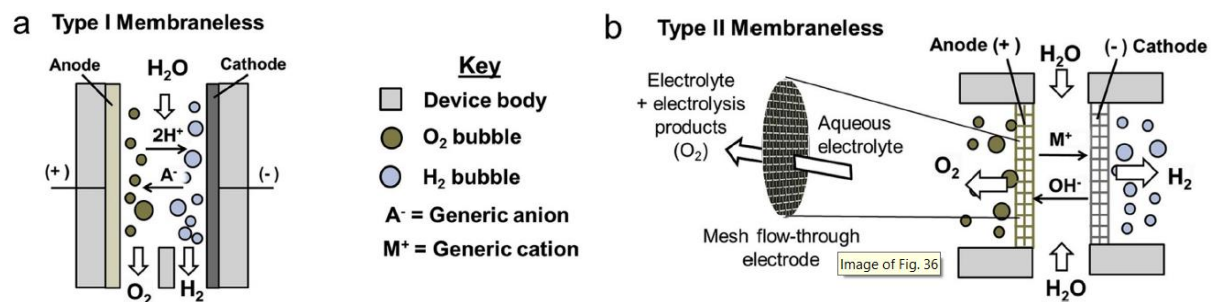


Figure 2.8 Cross-sectional view of flow-by, flow- through electrodes [2]

For the current project, non-integrated/modular type of solar hydrogen system has been selected due to its convenience and availability of individual components.

## 2.3 Solar Hydrogen Systems Examples

Ever since the world's first solar-powered hydrogen production plant became operational in 1990 in Southern Germany [5], hundreds of researchers and industries tried to develop different types of solar hydrogen systems. Multiple technologies of solar PV were tried to power the electrolyzer, ranging from amorphous Si solar cells to GaAs solar cells. Electrolyzers and fuel cells were mainly of alkaline or PEM technology, but a plethora of electrolytes and electrodes were tested in the alkaline versions. As the research advanced and as more people contributed towards this technology, the efficiency, life, stability, and cost have reasonable improved. Some examples of solar hydrogen systems from around the world are shown in Table 2.1. [1][2][4][6][7][8]

Table 2.1 Examples of solar hydrogen systems [1][2][4][6][7][8]

#	Components/Project Name	Solar Module/Cell	PV efficiency	Electrolyser	STHmax efficiency	Hydrogen Storage	Fuel Cell
[1]	PEM-EC, Solar cells	bifacial Si heterojunction	18.4% (30% albedo)	PEM	15.50%		-
		monofacial Si heterojunction	16.40%		13.70%		
[4]	-	InGaP/GaAs/GaInNAsSb triple-junction, highest STH	-	2 PEM	30%		-
		GaInP/GaAs/Ge multi-junction		10 cm <sup>2</sup> Ni foam electrodes in 1 M NaOH	22.40%		
		a-Si:H/a-Si:H/μc-Si:H triple junction		two Ti sheet electrodes loaded with Pt and IrO <sub>x</sub> catalysts	4.80%		
		Perovskite solar cells		bifunctional NiFe catalyst-loaded Ni foams as electrodes	12.30%		
		III-V solar cells		PEM	18%		
[6]	PV cell, photon-enhanced thermionic emission cell, SOEC	multi-junction GaAs PV cell	29.8% and 37.2% for triple-junction & quadruple-junction	Solid Oxide Electrolysis Cell	29.61%		-
[15]	FIRST (2000-2004)	1.4 kWp, monocrystalline Si		PEM, 1 kW		Metal hydrides, 30 bar, 70 Nm <sup>3</sup> volume cap, 248 kWh	PEM, 0.42 kW
	INTA (1989-97)	8.5 kWp	10% (avg)	Alkaline, 5 kW	7.05%	Metal hydrides - pressurized tanks, 200 bar, 24-9 Nm <sup>3</sup> volume cap, 85-32 kWh	PAFC-PEM, 10-7.5 kW
	PHEOBUS (1993-2003)	43 kWp		Alkaline, 26 kW		Pressurized tank, 120 bar, 3000 Nm <sup>3</sup> volume cap, 10638 kWh	PEM, 5.6 kW
	SAPHYS (1994-97)	5.6 kWp, monocrystalline Si		Alkaline, 5 kW		Pressurized tank, 200 bar, 120 Nm <sup>3</sup> volume cap, 426 kWh	PEM, 3 kW
	SCHATZ (1989-96)	9.2 kWp, monocrystalline Si		Alkaline, 6 kW	6.2% (avg)	Pressurized tank, 8 bar, 60 Nm <sup>3</sup> volume cap, 213 kWh	PEM, 1.5 kW
	Solar house (1992-95)	4.2 kWp		PEM 2 kW		Pressurized tank, 28 bar, 400 Nm <sup>3</sup> volume cap, 1418 kWh	PEM, 3.5 kW
	Solar hydrogen pilot plant (1990-92)	1.3 kWp	13% (avg)	Alkaline 0.8 kW	9.27% (avg)	Pressurized tank, 25 bar, 200 Nm <sup>3</sup> volume cap, 709 kWh	PAFC, 0.5 kW
	SWB (1989-96)	370 kWp, monocrystalline, polycrystalline and amorphous Si	9-13% (crystalline) & 5% (amorphous)	Alkaline 100 kW		Pressurized tank, 30 bar, 5000 Nm <sup>3</sup> volume cap, 17730 kWh	PAFC, 80 kW
	CEC (2007-)	5 kWp		Alkaline 3.35 kW		Metal hydrides, 14 bar, 5.4 Nm <sup>3</sup> volume cap, 19 kWh	PEM, 2.4 kW
[16]	solar cells, electrolyser, hydrogen storage tank, fuel cell			PEM	CHP fuel cell ~ 72%		PEM, 0.5 kW
[17]	PVT modules, electrolyser, fuel cell stack, battery, H <sub>2</sub> storage tank, H <sub>2</sub> compressor	PVT modules	9% (overall electrical energy efficiency)	PEM	14.5% (max net energy efficiency)		PEM

### 3. System Design and Selection of Components

Designing a fully functional solar hydrogen system would require an extensive design of the system. This can be done by ensuring that every subsystem is compatible with each other and contributes towards the ultimate goal of utilizing maximum possible amount of energy.

#### 3.1 System Design for Simulation

The solar hydrogen system is being developed by the logical combination of the following components and subsystems: solar PV array, MPPT algorithm, electrolyzer, hydrogen storage, fuel cell, load, thermally insulated system. The below flowchart shows the dependencies of each subsystem on others and the overall functioning of the system.

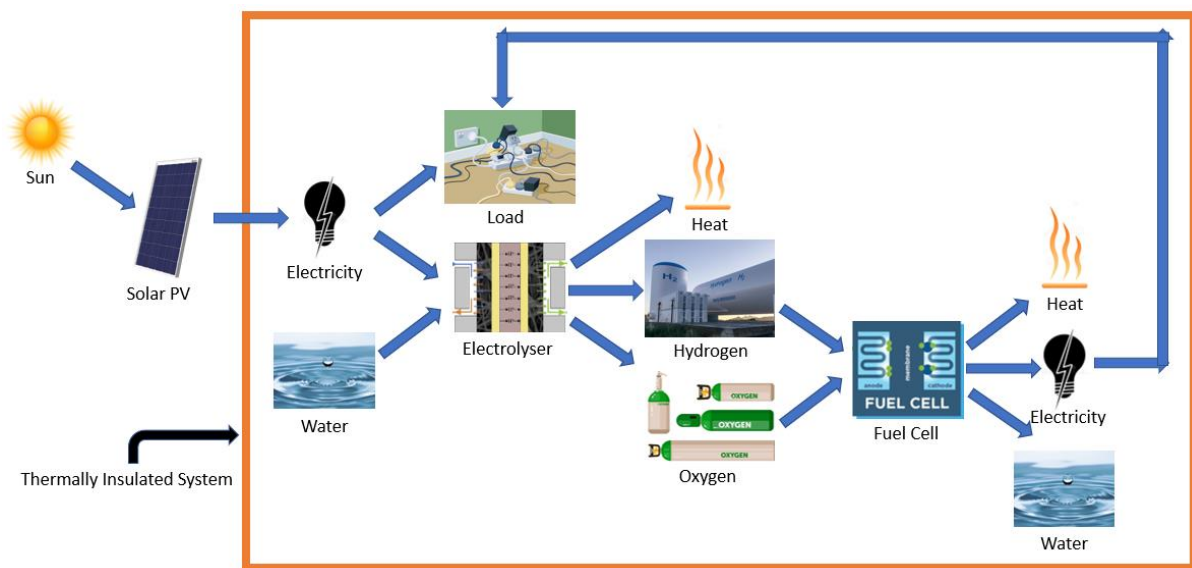


Figure 3.1 Flowchart of thermally insulated solar hydrogen system

Energy is provided to the system by sun rays. Incident solar radiation is captured by the solar panels and converted to electricity. This electricity is used to fulfil the load demand. System is designed in such a way that the electricity produced by solar PV in active sunshine hours is more than the peak load in the same time. This ensures that there is always electricity which is unused by the load. The unused energy drives the electrolyzer to produce hydrogen and oxygen, along with heat due to inefficiencies. Both the hydrogen and oxygen are stored in separate storage tanks/cylinders. When there is insufficient sunlight to meet the load demand or during non-sunshine hours, the stored hydrogen is used in fuel cell to produce electricity, water, and heat. Hydrogen can also be stored for long term usage in fuel cells in colder seasons with less or no sunlight. The thermally insulated space prevents heat loss to external environment, increasing the total energy utilization. All the heat released during the operation of electrolyzer and fuel cell is captured leading to higher internal temperature of the space.

Selection of components for each subsystem is discussed in the following subsections.



### 3.2 Solar PV Selection

Since the first ever solar cell made in 1883, a number of solar photovoltaic technologies have come up with varying advantages, applications, and costs. For the current study, the following technologies are considered: monocrystalline Si, polycrystalline Si, monocrystalline Si PERC, thin film, perovskite. Other technologies like Gallium Arsenide and III-V solar cells have been omitted from the comparison due to their extremely high cost in comparison to major technologies in the market.

In monocrystalline Si PERC, the acronym PERC stands for Passivated Emitter & Rear Contact. Mono Si is cheaper than mono Si PERC, but PERC cells are more efficient than the conventional mono Si. Hence the cost per unit energy becomes almost equal for both the technologies. So mono Si PERC is preferred over mono Si.

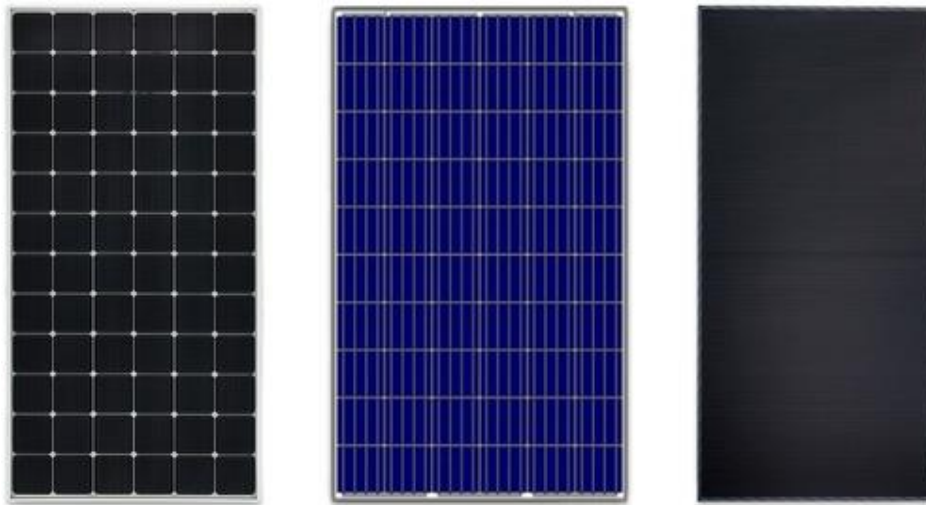


Figure 3.2 Monocrystalline, polycrystalline, and thin film solar modules. *Source: [internet](#)*

Monocrystalline and polycrystalline Si solar cells are very mature technologies due to decades of research and industrial applications. Polycrystalline Si cells are cheaper than their monocrystalline counterparts, but they are also less efficient in comparison. Polycrystalline cells perform worse in higher temperatures due to their higher temperature coefficients. Both of them have a very good life of about 25 years. The following tables help in comparison of monocrystalline Si PERC and polycrystalline Si solar cells. The data has been taken from the datasheets of Vikram Solar polycrystalline and monocrystalline solar cells.

Table 3.1 Vikram Solar Eldora polycrystalline Si PV modules. *Source: Vikram Solar datasheet*

Peak Power $P_{max}$ (W)	315	320	325	330	335	340
Max Voltage $V_{mpp}$ (V)	37.5	37.7	37.8	38	38.1	38.2
Max Current $I_{mpp}$ (V)	8.4	8.5	8.6	8.7	8.8	8.91
Open Circuit Voltage $V_{oc}$ (V)	45.8	46	46.2	46.3	46.5	46.7
Short Circuit Current $I_{sc}$ (A)	8.92	9.03	9.13	9.24	9.35	9.46
Module Efficiency (%)	16.23	16.49	16.75	17.01	17.26	17.52

Table 3.2 Vikram Solar Somera monocrystalline Si PERC PV modules. *Source: Vikram Solar datasheet*

Peak Power $P_{\max}$ (W)	365	370	375	380	385
Max Voltage $V_{\text{mpp}}$ (V)	39.8	40.0	40.1	40.2	40.3
Max Current $I_{\text{mpp}}$ (V)	9.17	9.26	9.36	9.46	9.56
Open Circuit Voltage $V_{\text{oc}}$ (V)	48.3	48.5	48.7	48.8	48.9
Short Circuit Current $I_{\text{sc}}$ (A)	9.73	9.84	9.94	10.04	10.14
Module Efficiency (%)	18.81	19.07	19.33	19.58	19.84

Both monocrystalline PERC and polycrystalline have same module area in the above tables. It can be concluded that monocrystalline Si PERC, although slightly expensive are much more efficient and perform better compared to polycrystalline Si solar modules.

Perovskite solar cells' efficiency has seen a steep rise in the last decade, reaching efficiencies greater than 25%. But none of these could be scaled up for commercial uses, they were lab-scale. Due to their low life and instability in ambient conditions like humidity and high cell temperature, perovskite solar cells are unsuitable for commercial applications yet.

Thin film solar cells have a very unique advantage of being foldable and look aesthetically good. Shading and high temperatures do not have a significant impact on this technology. But they are much lesser efficient compared to even polycrystalline Si solar cells. They also degrade faster than the crystalline solar cells, leading to shorter life-span.

On the basis of the above discussion, monocrystalline Si PERC solar cells have been finalized as the technology to be used for this project.

### 3.3 Electrolyzer Selection

An electrolyzer is a system that uses electricity to break water into hydrogen and oxygen. It also produces heat in the process due to the impossibility of 100% efficiency. There are mainly three types of electrolyzers namely alkaline, proton exchange membrane (PEM), and solid oxide. Depending on the electrolyte material being used in them, these electrolyzers vary slightly in their function.

Alkaline electrolyzers use a liquid electrolyte solution like potassium hydroxide (KOH) or sodium hydroxide (NaOH), and water ( $\text{H}_2\text{O}$ ). They are the oldest type of electrolyzers, dating back to the early 19<sup>th</sup> century, and well established too. Thus, it is the cheapest available option for electrolysis, cheaper than both PEM and Solid Oxide electrolyzers. They use non noble catalysts and have good long-term stability. But they suffer with low current densities, crossover of gases, and corrosive liquid electrolyte. [11]

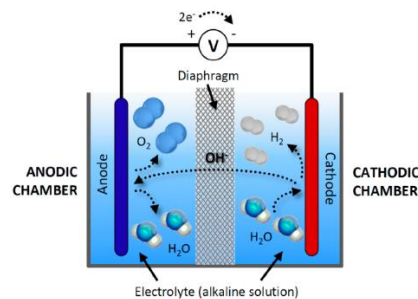


Figure 3.3 General depiction of an alkaline electrolyzer. *Source: internet*



PEM electrolyzers use a solid polymer electrolyte known as Proton Exchange Membrane or Polymer Electrolyte Membrane. Due to recent advancements in technology, the cost of PEM has also come down to competitive levels with alkaline electrolyzers. PEM technology has various advantages: it has a quick response ramp-up-and-down ability, and a vast dynamic operating range from 0 to 100% - meaning it is highly suitable for utilising additional renewable energy to generate hydrogen. They also have high current densities and high gas purity. But they too face a few problems like acidic corrosive environment, and high cost of components, and use of noble catalysts. Since this project aims to utilize the excess energy generated by solar panels to generate hydrogen, PEM has a clear advantage. [11]

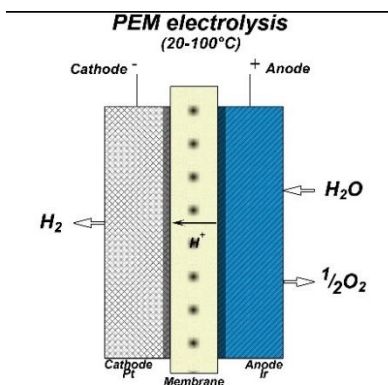


Figure 3.4 General depiction of a PEM electrolyzer. Source: [internet](#)

Solid Oxide Electrolyzers use solid ceramic material as electrolyte. These electrolyzers operate at a very high temperature, above 500° C. Due to this, they can be far more efficient than the other two electrolyzers. But due to their high operating temperatures, they cannot be used in this project as achieving those temperatures is not possible here. [11]

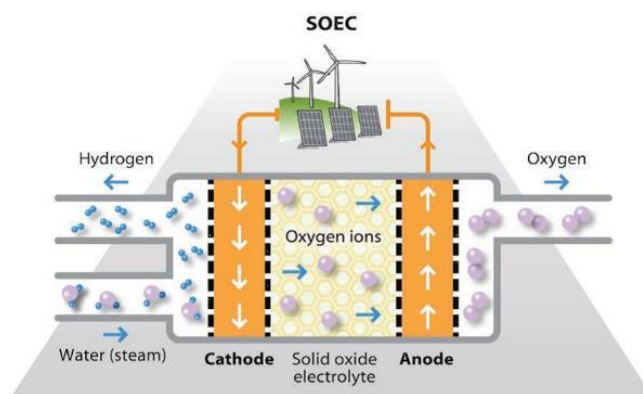


Figure 3.5 General depiction of a solid oxide electrolyzer. Source: [internet](#)

On the basis of the above discussion, PEM electrolyzer is chosen for this project to fulfil the role of electrolyzer.

### 3.4 Fuel Cell Selection

A typical fuel cell generates electrical energy using hydrogen as a fuel by reacting with oxygen to produce water and heat. There are many types of fuel cells, based on electrolyte, fuel, and electrode material. They include Polymer Electrolyte Membrane Fuel Cell (PEMFC), alkaline, solid polymer, sulfuric and phosphoric acid, solid oxide, molten carbonate fuel cells.



Alkaline fuel cells can easily start from cold temperatures, and operate usually at 60-80 °C. Noble and active catalysts are needed due to the lower operating. But a major problem of alkaline cells is due to the interaction of CO<sub>2</sub> with the base electrolyte. CO<sub>2</sub> is in the flow of oxygen input as input of oxygen is generally from direct air. Hence it requires some scrubbing mechanism to remove the 0.04% CO<sub>2</sub> in inlet air. [12]

Sulfuric and phosphoric acid fuel cells are not so intolerant to CO<sub>2</sub>, allowing the usage direct air and slightly impure hydrogen. But there exists the problem of corrosion which imposes restrictions on the materials for catalysts and electrodes. These operate at a temperature around 200° C that requires a platinum catalyst, which is susceptible to CO-poisoning at this temperature. Due to the indecent performance of the air electrode, the efficiencies of acid cells are lower compared to alkaline cells. [12]

In PEMFC, the electrolyte is a solid polymer layer which allows transmission of protons. Due to the limitations of membrane's thermal properties, PEMFCs operate at relatively lower temperature around 90 °C. They are also prone to contamination by CO, leading to a considerable reduction in efficiency. Additionally, cooling and output water management is essential for it to function appropriately. [21]

In solid polymer fuel cells, an example is using methanol directly as a fuel. It is still in development phase, with prototypes. Main problems include the lower electrochemical activity of CH<sub>3</sub>OH in comparison to hydrogen, leading to lower cell efficiencies. Also, due to the miscibility of methanol in water, it might lead to crossing the water-saturated membrane causing corrosion and output gas challenges. [12]

The electrolyte of molten carbonate fuel cell is a molten mixture of K<sub>2</sub>CO<sub>3</sub> and Li<sub>2</sub>CO<sub>3</sub> which allows movement of CO<sub>3</sub><sup>2-</sup> ions from cathode to anode. They operate at around 850 °C enabling the usage of nickel as catalyst. [12]

SOFCS are built wholly using solid-state materials with an electrolyte made of ion-conducting oxide ceramic. They operate at around 900-1000° C. They have many advantages over other fuel cell configurations: easier management of electrolyte, best efficiency among all the fuel cell technologies (50-60%), and internal reforming of hydrocarbon fuels can be done for CHP (Combined Heat & Power) uses. But they are very expensive to manufacture due to the requirement of costly high temperature alloys needed for the BOP structures. [12]

Based on above discussion, PEM is chosen for this project to fulfil the role of fuel cell.

### **3.5 Passive Solar Tent Design**

The main aim of the thermally insulated system is to utilise the maximum possible heat produced during the operation of electrolyzer and fuel cell. Adding passive solar design would lead to greater thermal comfort and higher internal temperatures of the space. Hence, combining both passive solar tent design and thermal insulation of the system would give the best possible results.

#### **3.5.1 South-Facing Wall Design**

The system being developed can be considered as a single room. Passive space heating systems can be divided into direct, indirect, and isolated gain systems.

In a direct gain system, the heated space is directly exposed to sunlight, which is converted to heat by absorbing surfaces. Greenhouses are direct gain systems. Figure 3.6 shows an example of a direct gain system. [10]

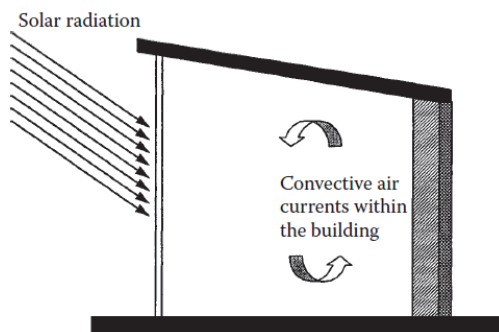


Figure 3.6 Direct gain system [10]

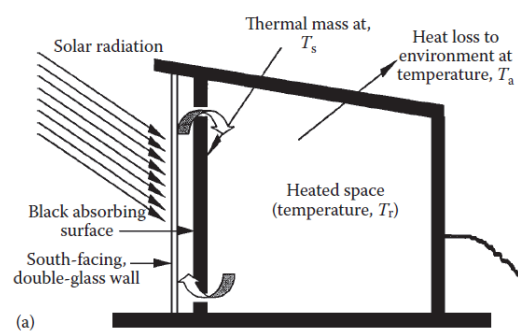


Figure 3.7 Indirect gain system [10]

In an indirect gain system, a heat absorbing mass is present in between the internal space and the glass. This mass absorbs the irradiation from sun and retains it as heat. Examples include Trombe wall and solar wall. Figure 3.7 shows an example of an indirect gain system with a thermal storage wall.

The isolated gain is a modification of the indirect system with a definite thermal barrier between thermal storage and internal space by insulation or physical barrier. An example of this is a thermosyphon loop often used to heat domestic water. This loop is used to form a thermal storage wall or roof. [10]

Among the three systems, the indirect gain configuration is better for this project as it has a time lag in between solar radiation and heating of internal space, leading to better warmth during non-sunshine hours.

### 3.5.2 Internal Design

The passive solar tent is given the shape of a semi-cylindrical tent. It is divided into two halves with a partition in between – the first half is south-facing wall, the second half is the north-facing facility. [13]



Figure 3.8 Design of the solar tent [13]

The south-facing wall allows sunlight inside which heats up the tent. It can be used as a living space during daytime. The partition in between has thermally insulating door and windows. The partition acts as the thermal mass which stores heat from sun light during daytime and releases it towards the north partition during the night. The north-facing wall is made up of multiple thick layers of insulating materials, whose number of layers are variable

based on the season and requirement. This half can be utilized as a sleeping chamber during night time. The cylindrical-shaped roof leads to the least surface area among all shapes, which helps in minimizing the heat loss through walls.

During daytime, the windows and door of the partition are kept open to allow the passage of heat from the south partition to the north partition. During night, the windows and the door are closed to prevent loss of heat from the north side.

The solar tent is made up of re-arrangeable parts weighing less than 30 kgs per part. This modular design allows for convenient transportation and easier assembling of the tent. The cost of a solar tent is almost half of the cost of other alternatives available such as the metallic containers, which do not have passive heating properties, and are smaller in area. [13]

## 4. Modelling of Solar Hydrogen System

To analyze the performance of the system being developed, it is very important to have insights about how the system will behave under various operating conditions. Before directly developing a prototype, online modelling and simulation gives an idea of the possible scenarios and can help in understanding the limitations and problems in the system. For this project, modelling of solar PV, electrolyzer, fuel cell, hydrogen storage, passive solar tent, and load is done.

### 4.1 Solar PV Modelling

Solar radiation is highly time dependent and varies from location to location. Hence, it is extremely important to capture the variability in the incoming solar energy over the 24 hours in a day and over the 12 months in a year. This will give a good idea of the minimum and maximum capacity of solar PV array, electrolyzer, fuel cell, and hydrogen storage capacities.

Mathematical modelling of Solar PV can be done in two ways. The first method deals with currents and voltages and results in very detailed and exhaustive models. This makes it difficult to understand and increases the computational requirement and complexity of the model. But it also produces very accurate models in comparison to real life data. The second method deals with energy or power, making it much simpler and easier to understand. This reduces the computational requirement leading to lesser complex models. But they are less accurate than the models produced by the first method.

The current model is based on the first method, adopted from [9]. A solar PV cell can be represented by electrical circuit in Figure 4.1. Shunt resistance is neglected since it is very large.

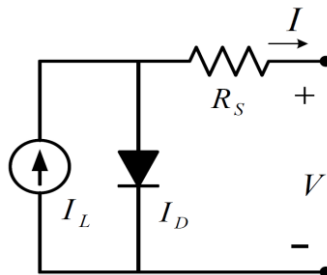


Figure 4.1 Representative circuit diagram for a solar cell [9]

From the above circuit with a diode, current source and resistor, the load current can be calculated as follows:

$$I = I_L - I_D = I_L - I_o \left[ \exp \left( \frac{V + IR_s}{\alpha} \right) - 1 \right] \quad (4.1)$$

Here,  $I$  represents the load current (A),  $I_L$  represents the light current or photocurrent (A),  $I_D$  represents the diode current (A),  $I_o$  represents the saturation current (A),  $V$  represents the output voltage (V),  $R_s$  represents the series resistance ( $\Omega$ ),  $\alpha$  represents the thermal voltage timing completion factor (V). It can be noted that the light current is same as the short circuit current  $I_{SC}$  (A).

$$I_L = I_{SC} \quad (4.2)$$

This is a four-parameter model, where  $I_{SC}$ ,  $I_o$ ,  $R_s$ , and  $\alpha$  need to be determined.  $I_L$  and  $I_{SC}$  are used interchangeably here. Light current can be given as

$$I_L = \frac{\phi}{\phi_{ref}} [I_{L,ref} + \mu_{I,SC} (T_C - T_{C,ref})] \quad (4.3)$$

Here,  $\phi$  represents the irradiance ( $\text{W/m}^2$ ),  $\phi_{ref}$  represents the reference irradiance ( $1000 \text{ W/m}^2$ ),  $I_{L,ref}$  represents the photocurrent at  $1000 \text{ W/m}^2$  and  $25^\circ \text{C}$ ,  $\mu_{I,SC}$  represents the temperature coefficient of  $I_{SC}$  ( $\text{A}/^\circ\text{C}$ ),  $T_C$  represents the solar cell temperature,  $T_{C,ref}$  represents the reference temperature ( $25^\circ \text{C}$ ). The reference conditions ( $1000 \text{ W/m}^2$  and  $25^\circ \text{C}$ ) are referred as Standard Test Conditions (STC)

Saturation current at any temperature can be expressed as a function of its reference value as

$$I_0 = I_{0,ref} \left( \frac{T_{C,ref} + 273}{T_C + 273} \right)^3 \exp \left[ \frac{e_{gap} N_s}{q \alpha_{ref}} \left( 1 - \frac{T_{C,ref} + 273}{T_C + 273} \right) \right] \quad (4.4)$$

Here,  $I_{0,ref}$  represents the saturation current at STC,  $e_{gap}$  represents the bandgap of the solar cell material ( $1.12 \text{ eV}$  for Silicon),  $N_s$  represents the number of cells connected in series,  $q$  represents the charge of an electron ( $1.6 \times 10^{-19} \text{ C}$ ),  $\alpha_{ref}$  represents the value of  $\alpha$  at STC.

$I_{0,ref}$  is given by

$$I_{0,ref} = I_{L,ref} \exp \left( - \frac{V_{oc,ref}}{\alpha_{ref}} \right) \quad (4.5)$$

Here,  $V_{oc,ref}$  represents the open circuit voltage at STC.

$\alpha_{ref}$  is given by

$$\alpha_{ref} = \frac{2V_{mp,ref} - V_{oc,ref}}{\frac{I_{sc,ref}}{I_{sc,ref} - I_{mp,ref}} + \ln \left( 1 - \frac{I_{mp,ref}}{I_{sc,ref}} \right)} \quad (4.6)$$

Here,  $V_{mp,ref}$  represents the voltage at maximum power point at STC,  $I_{mp,ref}$  represents the current at maximum power point at STC,  $I_{sc,ref}$  represents the short circuit current at STC.

$\alpha$  is related to temperature as follows

$$\alpha = \frac{T_C + 273}{T_{C,ref} + 273} \alpha_{ref} \quad (4.7)$$

$R_s$  can be estimated by the following equation

$$R_s = \frac{\alpha_{ref} \ln \left( 1 - \frac{I_{mp,ref}}{I_{sc,ref}} \right) + V_{oc,ref} - V_{mp,ref}}{I_{mp,ref}} \quad (4.8)$$

$V_{oc}$  can be calculated as

$$V_{oc} = \alpha \ln \left( \frac{I_{sc} + I_o}{I_o} \right) \quad (4.9)$$

From Eq. (4.1), voltage,  $V$  can be written in terms of current,  $I$  as in Eq. (4.10).

$$V = \alpha \ln \left( \frac{I_{sc} - I}{I_o} + 1 \right) - IR_s \quad (4.10)$$

Power,  $P$  is given by the following equation

$$P = VI \quad (4.11)$$

For maximum power, differential of power with respect to current should be zero. Substituting the value of  $V$  from Eq. (4.10) into Eq. (4.11) and differentiating gives the following relation

$$\frac{dP}{dI} = \alpha \left( \frac{I}{I - I_{sc} - I_o} + \ln \left( \frac{-I + I_{sc} + I_o}{I_o} \right) \right) - 2IR_s = 0 \quad (4.12)$$

To calculate the current, Newton Raphson method has been implemented as follows

$$f(I) = \alpha \left( \frac{I}{I - I_{sc} - I_o} + \ln \left( \frac{-I + I_{sc} + I_o}{I_o} \right) \right) - 2IR_s \quad (4.13)$$

$$f'(I) = \alpha \left( \frac{I - 2I_{sc} - 2I_o}{(I - I_{sc} - I_o)^2} \right) - 2R_s \quad (4.14)$$

$$x_{n+1} = x_n - \frac{f(x_n)}{f'(x_n)} \quad (4.15)$$

Taking an appropriate initial value of  $x_o$  (close to  $I_{sc}$ ), Eq. (4.15) is iterated 500 times in MATLAB function to converge to the value of  $I_{mp}$ , the value of current at maximum power. The obtained value of  $I_{mp}$  is used to calculate  $V_{mp}$  by using Eq. (4.10).

In real life situations, it is difficult to calculate the cell temperature as it requires specialized equipment. The ambient temperature data is more easily available. Hence, an equation that relates ambient temperature to the cell temperature will increase the convenience of the model.

$$T_c = T_{amb} + (NOCT - 20^\circ C) \frac{\phi}{800} \quad (4.16)$$

Among all the above mentioned parameters,  $I_{L,ref}$  (also referred as  $I_{sc,ref}$ ),  $V_{oc,ref}$ ,  $I_{mp,ref}$ ,  $V_{mp,ref}$ ,  $\mu_{I,sc}$ ,  $N_s$ ,  $NOCT$  are provided by the manufacturer in the datasheet. These equations have been used to create a Simulink model (Figure 4.2) to generate I-V characteristic curves for a solar module. This model takes the ambient temperature (K) and the solar irradiance ( $W/m^2$ ) as input and gives current and voltage at maximum power, which can be used to calculate the maximum power output for the given conditions.

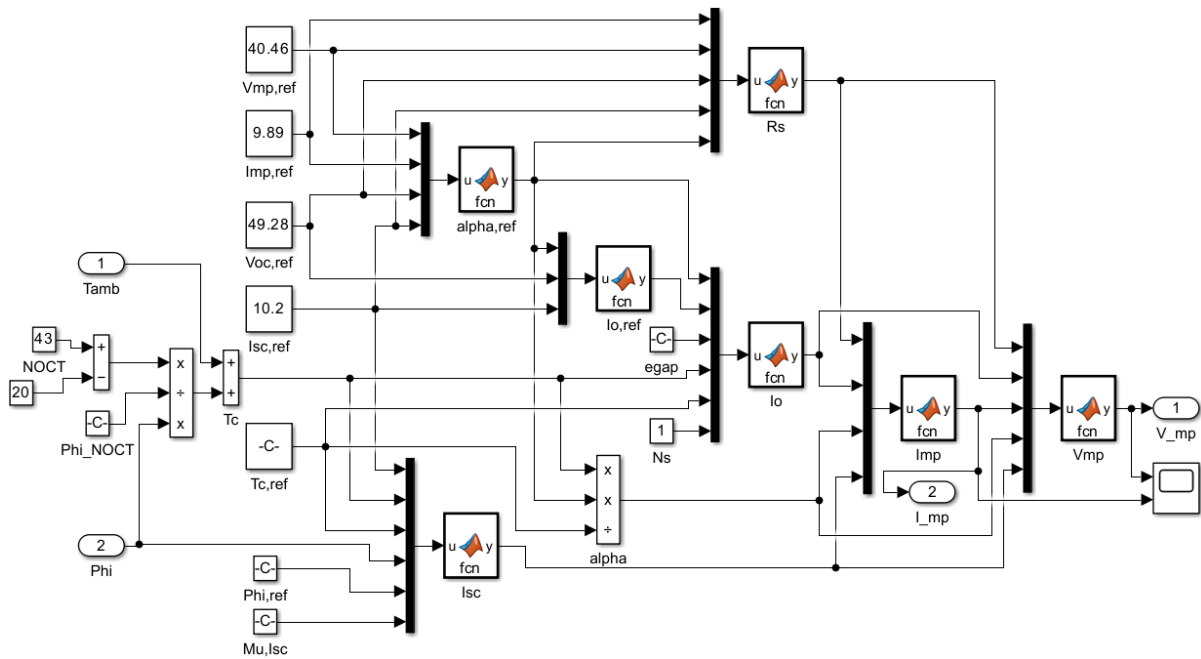


Figure 4.2 Simulink model of the solar module

The parameters shown in the Simulink model are adopted from the Polycab monocrystalline PERC 72 cell 5BB PV module. Technical specifications of the PV module at STC are given in Table 4.1.

Table 4.1 Technical specifications of Polycab solar module. *Source: Polycab Manufacturer Datasheet*

Model	PIL 400HM
Maximum Power, $P_{max}$ (W)	400
Open Circuit Voltage, $V_{oc}$ (V)	49.28
Short Circuit Current, $I_{sc}$ (A)	10.2
Voltage at Maximum Power, $V_{mp}$ (V)	40.46
Current at Maximum Power, $I_{mp}$ (A)	9.89
Module Efficiency (%)	20.12
Coefficient of Short Circuit Current, $\mu_{Isc}$ (%/°C)	0.05
Nominal Operating Cell Temperature, $NOCT$ (°C)	43

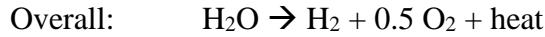
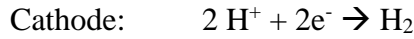
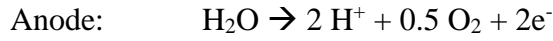
## 4.2 Electrolyzer Modelling

The amount of hydrogen produced from electrolysis depends on multiple factors like electrolyzer current, operating voltage, input power, electrode area, temperature, pressure. The excess renewable energy should be able to drive the electrolysis reaction. This can be ensured by using appropriate DC-DC converters (buck converters) to output a voltage sufficient to start electrolysis. Generally, the industrial electrolyzers are operated in a range of voltage between 1.8 - 2.2 V. Ideally, the electrolyzer should run at 1.23 V, but it cannot run at 1.23 V practically due to multiple losses. These include ohmic overpotential, concentration overpotential, and activation overpotential.



Mathematical modelling of an electrolyzer has been done in many ways over the years. Parameters like partial pressure and molar flow rate of water, hydrogen, and oxygen, current density, active area, and the above listed overpotentials have been used to develop robust models to represent a PEM electrolyzer closely.

The reactions occurring at the anode and the cathode of a PEM electrolyzer are as follows



The Simulink model for electrolyzer, adopted from [14], is developed from four modular components (divided into five Simulink subsystems), namely anode, cathode, membrane, and voltage.

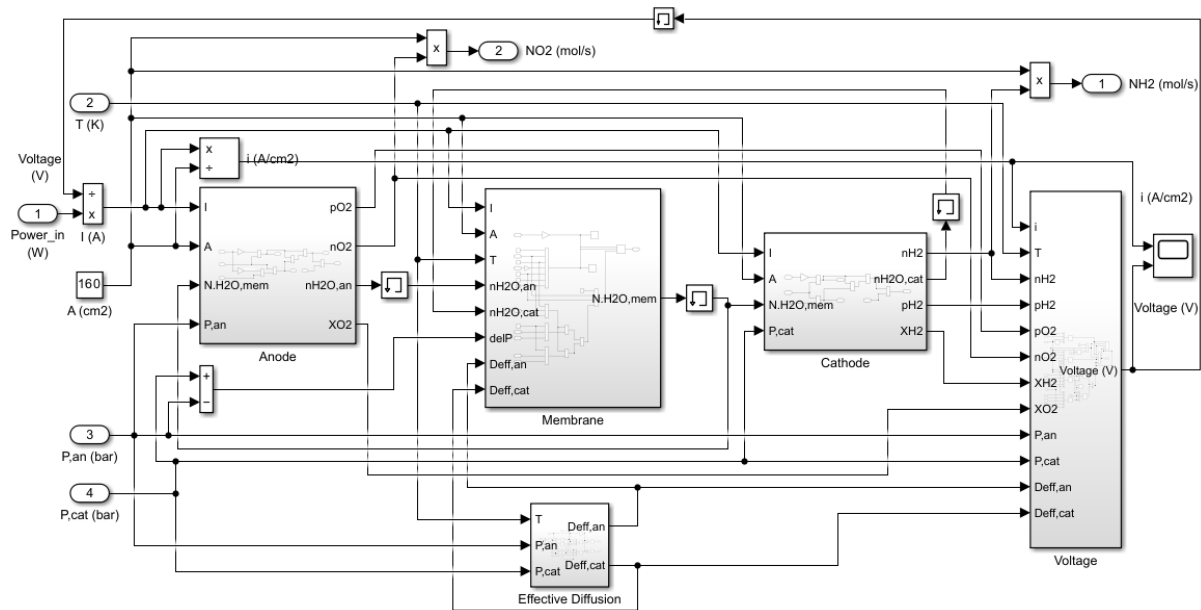


Figure 4.3 Simulink model of the electrolyzer

#### 4.2.1 Anode

The anode outputs the oxygen and water flow rates along with their partial pressures. The flow rates are guided by the following equations

$$\frac{dN_{O_2}}{dt} = N_{O_2}^{in} - N_{O_2}^{out} + N_{O_2}^{gn} \quad (4.17)$$

$$\frac{dN_{H_2O}}{dt} = N_{H_2O}^{in} - N_{H_2O}^{out} - N_{H_2O}^{cons} - N_{H_2O}^{mem} \quad (4.18)$$

Where  $N_{O_2}^{in}$ ,  $N_{H_2O}^{in}$ ,  $N_{O_2}^{out}$ ,  $N_{H_2O}^{out}$  are the inlet and outlet molar flow rates of  $\text{O}_2$  and  $\text{H}_2\text{O}$  respectively for anode,  $N_{O_2}^{gn}$  is the oxygen generation rate at anode,  $N_{H_2O}^{cons}$  is the water consumption rate,  $N_{H_2O}^{mem}$  is the membrane water flow rate.

Molar flow rates of oxygen and water can be calculated from Faraday's law as follows

$$N_{O_2}^{gn} = \frac{I}{4F} \quad (4.19)$$

$$N_{H_2O}^{cons} = \frac{I}{2F} \quad (4.20)$$

The net anode molar flux rate of water is given as

$$n_{H_2O}^{an} = \frac{N_{H_2O}^{mem} + N_{H_2O}^{cons}}{A} \quad (4.21)$$

The net anode molar flux rate of oxygen is given as

$$n_{O_2} = \frac{N_{O_2}^{gn}}{A} = \frac{I}{4FA} \quad (4.22)$$

The mole fraction and partial pressure of oxygen is given as

$$X_{O_2} = \frac{n_{O_2}}{n_{O_2} + n_{H_2O}^{an}} \quad (4.23)$$

$$p_{O_2} = X_{O_2} P_{an} \quad (4.24)$$

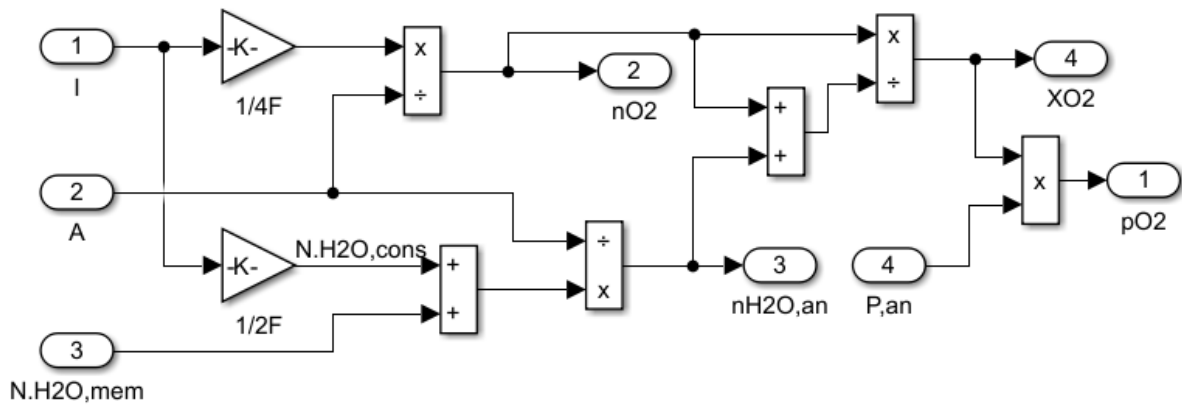


Figure 4.4 Simulink model of the anode subsystem in the electrolyzer

## 4.2.2 Cathode

The anode outputs the hydrogen and water flow rates along with their partial pressures. The flow rates are guided by the following equations

$$\frac{dN_{H_2}}{dt} = N_{H_2}^{in} - N_{H_2}^{out} + N_{H_2}^{gn} \quad (4.25)$$

$$\frac{dN_{H_2O}}{dt} = N_{H_2O}^{in} - N_{H_2O}^{out} + N_{H_2O}^{mem} \quad (4.26)$$

Molar flow rate of hydrogen can be calculated from Faraday's law as follows

$$N_{H_2}^{gn} = \frac{I}{2F} \quad (4.27)$$

The cathode molar flux rate of hydrogen and water is given as

$$n_{H_2} = \frac{N_{H_2}^{gn}}{A} = \frac{I}{2FA} \quad (4.28)$$

$$n_{H_2O}^{cat} = \frac{N_{H_2O}^{mem}}{A} \quad (4.29)$$

The mole fraction and partial pressure of oxygen is given as

$$X_{H2} = \frac{n_{H2}}{n_{H2} + n_{H2O}^{cat}} \quad (4.30)$$

$$p_{H2} = X_{H2} P_{cat} \quad (4.31)$$

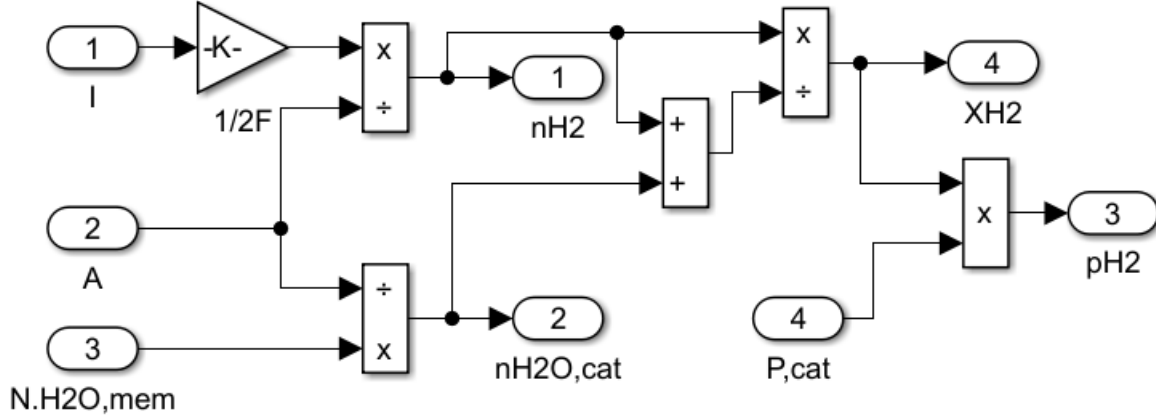


Figure 4.5 Simulink model of the cathode subsystem in the electrolyzer

### 4.2.3 Membrane

The resultant water flow rate through the membrane can be divided into three components – hydraulic pressure effect, diffusion, and electro-osmotic drag.

$$N_{H2O}^{mem} = N_{H2O}^{diff} + N_{H2O}^{eod} - N_{H2O}^{pe} \quad (4.32)$$

The molar flow rate due to diffusion is given by integrating Fick's law between two interfaces as

$$N_{H2O}^{diff} = \frac{AD_w}{\delta_{mem}} (C_{H2O,mem}^{cat} - C_{H2O,mem}^{an}) \quad (4.33)$$

Where  $D_w$  is the diffusion coefficient of water in the membrane,  $\delta_{mem}$  is the membrane thickness,  $C_{H2O,mem}^{cat}$  and  $C_{H2O,mem}^{an}$  are the concentrations of water on cathode and anode sides of the membrane respectively. These concentrations are expressed as the electrode channel water concentrations

$$C_{H2O,mem}^{an} = C_{H2O,ch}^{an} - \frac{\delta_{el}^{an} n_{H2O}^{an}}{D_{eff}^{an}} \quad (4.34)$$

$$C_{H2O,mem}^{cat} = C_{H2O,ch}^{cat} + \frac{\delta_{el}^{cat} n_{H2O}^{cat}}{D_{eff}^{cat}} \quad (4.35)$$

Where  $\delta_{el}^{an}$ ,  $\delta_{el}^{cat}$  are the anode and cathode thicknesses,  $D_{eff}^{an}$ ,  $D_{eff}^{cat}$  are the effective binary diffusion coefficients at the anode and cathode respectively. These effective diffusion coefficients can be expressed as

$$\frac{1}{D_{eff}^{an}} = \frac{\varepsilon}{\xi} \left( \frac{1}{D_{eff}^{O2-H2O}} + \frac{1}{D_{eff}^{H2O,K}} \right) \quad (4.36)$$

$$\frac{1}{D_{eff}^{cat}} = \frac{\varepsilon}{\xi} \left( \frac{1}{D_{eff}^{H_2-H_2O}} + \frac{1}{D_{eff}^{H_2O,K}} \right) \quad (4.37)$$

Where  $\varepsilon$  is the electrode porosity,  $\xi$  is the tortuosity,  $D_{eff}^{O_2-H_2O}$ ,  $D_{eff}^{H_2-H_2O}$  are the effective molecular diffusion coefficients for the  $O_2$ - $H_2O$  and  $H_2$ - $H_2O$  binary systems,  $D_{eff}^{H_2O,K}$  is the effective Knudsen diffusion coefficient for  $H_2O$  which is given as

$$D_{eff}^{H_2O,K} = \frac{4}{3} r \sqrt{\frac{8RT}{\pi M_{H_2O}}} \quad (4.38)$$

Where  $r$  is the average pore radius,  $M_{H_2O}$  is the molar weight of water.  $D_{eff}^{O_2-H_2O}$  and  $D_{eff}^{H_2-H_2O}$  can be expressed using the Chapman-Enskog theory of the ideal gas as

$$D_{eff}^{O_2-H_2O} = 0.00133 \left( \frac{1}{M_{O_2}} + \frac{1}{M_{H_2O}} \right)^{1/2} \frac{T^{3/2}}{P_{an} \sigma_{O_2-H_2O}^2 \Omega_D} \quad (4.39)$$

$$D_{eff}^{H_2-H_2O} = 0.00133 \left( \frac{1}{M_{H_2}} + \frac{1}{M_{H_2O}} \right)^{1/2} \frac{T^{3/2}}{P_{cat} \sigma_{H_2-H_2O}^2 \Omega_D} \quad (4.40)$$

Where  $M_{O_2}$  and  $M_{H_2}$  are the molar weights of oxygen and hydrogen,  $\sigma_{O_2-H_2O}$  and  $\sigma_{H_2-H_2O}$  are the average molecular radius of  $O_2$ - $H_2O$  and  $H_2$ - $H_2O$ ,  $\Omega_D$  is diffusion collision integral. These quantities can be expressed as

$$\Omega_D = \frac{1.06}{\tau^{0.156}} + \frac{0.193}{\exp(0.476\tau)} + \frac{1.036}{\exp(1.53\tau)} + \frac{1.765}{3.894\tau} \quad (4.41)$$

$$\sigma_{O_2-H_2O} = \frac{\sigma_{O_2} + \sigma_{H_2O}}{2} \quad (4.42)$$

$$\sigma_{H_2-H_2O} = \frac{\sigma_{H_2} + \sigma_{H_2O}}{2} \quad (4.43)$$

$$\tau_{O_2-H_2O} = \frac{kT}{\varepsilon_{O_2-H_2O}} \quad (4.44)$$

$$\tau_{H_2-H_2O} = \frac{kT}{\varepsilon_{H_2-H_2O}} \quad (4.45)$$

$$\varepsilon_{O_2-H_2O} = \sqrt{\varepsilon_{O_2} \varepsilon_{H_2O}} \quad (4.46)$$

$$\varepsilon_{H_2-H_2O} = \sqrt{\varepsilon_{H_2} \varepsilon_{H_2O}} \quad (4.47)$$

Where  $\varepsilon_{O_2-H_2O}$  and  $\varepsilon_{H_2-H_2O}$  are Lennard-Jones energies, the values of  $\sigma_{O_2}$ ,  $\sigma_{H_2}$ , and  $\sigma_{H_2O}$  are 3.467 Å, 2.827 Å, and 2.641 Å respectively.  $\varepsilon_i/k$  for  $O_2$ ,  $H_2$ , and  $H_2O$  are 106.7 K, 59.7 K, and 809.1 K respectively. Solving Eq. (4.36) to Eq. (4.47) gives the values of  $D_{eff}^{O_2-H_2O}$  and  $D_{eff}^{H_2-H_2O}$ .

The electrode channel water concentrations are given as

$$C_{H_2O,ch}^{an} = \frac{\rho_{H_2O}(T_{an})}{M_{H_2O}} \quad (4.48)$$

$$C_{H_2O,ch}^{cat} = \frac{\rho_{H_2O}(T_{cat})}{M_{H_2O}} \quad (4.49)$$

Where  $\rho_{H_2O}$  is the density of water,  $T_{an}$  and  $T_{cat}$  are the anode and cathode temperatures, which are considered to be the same for the current model.

Substituting Eq. (4.48) and Eq. (4.49) into Eq. (4.34) and Eq. (4.35) and subsequently substituting these equations into Eq. (4.33) gives

$$N_{H_2O}^{diff} = \frac{AD_w}{\delta_{mem}} \left( \left( \frac{\rho_{H_2O}(T_{cat})}{M_{H_2O}} + \frac{\delta_{el}^{cat} n_{H_2O}^{cat}}{D_{eff}^{cat}} \right) - \left( \frac{\rho_{H_2O}(T_{cat})}{M_{H_2O}} - \frac{\delta_{el}^{an} n_{H_2O}^{an}}{D_{eff}^{an}} \right) \right) \quad (4.50)$$

The water molar flow rate due to electro-osmotic drag can be expressed as

$$N_{H_2O}^{eod} = \frac{n_d I}{F} \quad (4.51)$$

The water flow rate due to hydraulic pressure effect can be evaluated by Darcy's law as

$$N_{H_2O}^{pe} = \frac{K_{Darcy} A \rho_{H_2O} \Delta P}{\delta_{mem} \mu_{H_2O} M_{H_2O}} \quad (4.52)$$

Substituting Eq. (4.50), Eq. (4.51), and Eq. (4.52) into Eq. (4.32) gives the value of  $N_{H_2O}^{mem}$ .

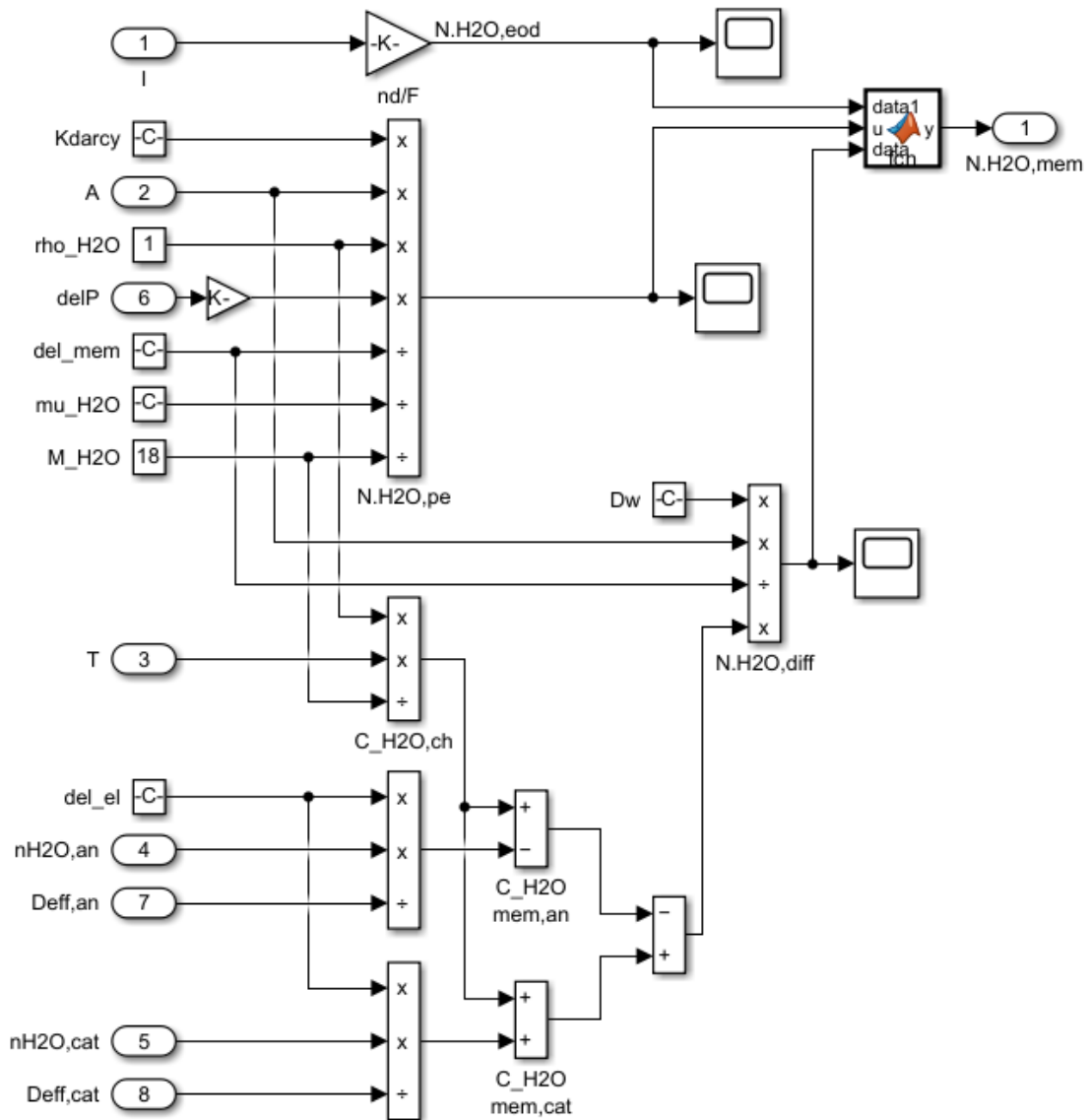


Figure 4.6 Simulink model of the membrane subsystem in the electrolyzer

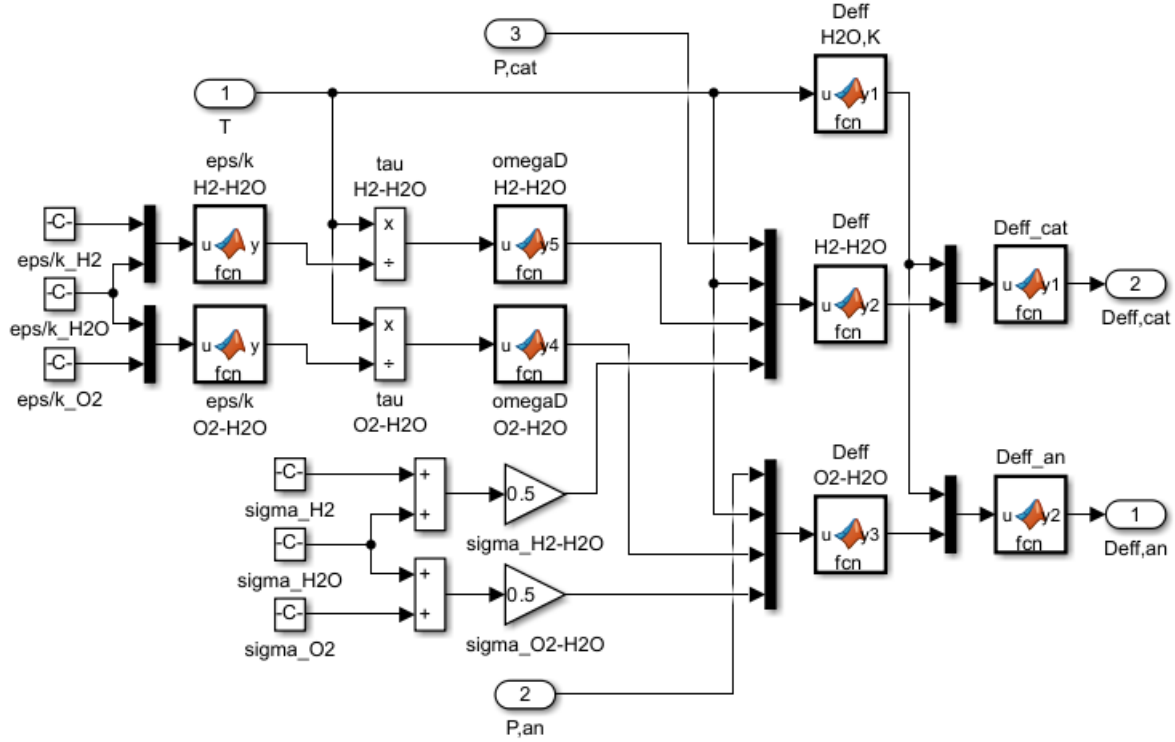


Figure 4.7 Simulink model of the effective diffusion subsystem in the electrolyzer

#### 4.2.4 Voltage

The operating voltage,  $V$ , of an electrolyzer can be divided into four components: open circuit voltage,  $V_{oc}$ , activation overpotential,  $V_{act}$ , ohmic overpotential,  $V_{ohm}$ , and concentration overpotential,  $V_{con}$ .

$$V = V_{oc} + V_{act} + V_{ohm} + V_{con} \quad (4.53)$$

From the Nernst equation, the open circuit voltage can be expressed as

$$V_{oc} = E_o + \frac{RT}{2F} \left( \ln \left( \frac{p_{H_2} \sqrt{p_{O_2}}}{a_{H_2O}} \right) \right) \quad (4.54)$$

$E_o$  varies with temperature as

$$E_o = 1.229 - 0.85 \times 10^{-3} (T - 298) \quad (4.55)$$

Activation overpotential is given as

$$V_{act} = V_{act}^{an} + V_{act}^{cat} \quad (4.56)$$

$$V_{act}^{an} = \frac{RT}{\alpha_{an} F} \operatorname{arcsinh} \left( \frac{i}{2i_{o,an}} \right) \quad (4.57)$$

$$V_{act}^{cat} = \frac{RT}{\alpha_{cat} F} \operatorname{arcsinh} \left( \frac{i}{2i_{o,cat}} \right) \quad (4.58)$$

Eq. (4.57) and Eq. (4.58) can be substituted in Eq. (4.56) to find  $V_{act}$ .

Concentration overpotential is given as

$$V_{con} = V_{con}^{an} + V_{con}^{cat} \quad (4.59)$$

$$V_{con}^{an} = \frac{RT}{4F} \ln \left( \frac{C_{O_2}^{mem}}{C_{O_2,0}^{mem}} \right) \quad (4.60)$$

$$V_{con}^{cat} = \frac{RT}{2F} \ln \left( \frac{C_{H_2}^{mem}}{C_{H_2,0}^{mem}} \right) \quad (4.61)$$

Where  $C_{O_2}^{mem}$  and  $C_{H_2}^{mem}$  are the  $O_2$  and  $H_2$  concentrations at the electrode-membrane interface,  $C_{O_2,0}^{mem}$  and  $C_{H_2,0}^{mem}$  are the working conditions taken as reference, whose values are taken from [19].

$$C_{H_2}^{mem} = C_{H_2}^{ch} - \frac{\delta_{el}^{cat} n_{H_2}}{D_{eff}^{cat}} \quad (4.62)$$

$$C_{O_2}^{mem} = C_{O_2}^{ch} - \frac{\delta_{el}^{an} n_{O_2}}{D_{eff}^{an}} \quad (4.63)$$

$$C_{H_2}^{ch} = \frac{P_{cat} X_{H_2}}{RT} \quad (4.64)$$

$$C_{O_2}^{ch} = \frac{P_{an} X_{O_2}}{RT} \quad (4.65)$$

Substituting Eq. (4.64) and Eq. (4.65) into Eq. (4.62) and Eq. (4.63) and subsequently substituting them into Eq. (4.60), Eq. (4.61), and Eq. (4.59) gives the value of concentration overpotential.

Ohmic overpotential is mainly due to the membrane, which can be expressed as

$$V_{ohm}^{mem} = \frac{\delta_{mem} I}{A \sigma_{mem}} \quad (4.66)$$

Where  $\delta_{mem}$  is the thickness of PEM and  $\sigma_{mem}$  is the conductivity of PEM, which can be expressed as

$$\sigma_{mem} = (0.005139\lambda - 0.00326) \exp \left( 1268 \left( \frac{1}{303} - \frac{1}{T} \right) \right) \quad (4.67)$$

Evaluating Eq. (4.54) to Eq. (4.67) gives the values of the four components of the operating voltage, which can be found from Eq. (4.53).

Values of parameters used in this model are given in Table 4.2.

Table 4.2 Parameters used in the electrolyzer model [14]

Parameter	Value	Parameter	Value
A (cm <sup>2</sup> )	160	$\xi$	4
$\delta_{mem}$ (cm)	0.0254	F (C mol <sup>-1</sup> )	96485
$\delta_{el}$ (cm)	0.008	R (J mol <sup>-1</sup> K <sup>-1</sup> )	8.314
$\rho_{el}$ ( $\Omega$ cm)	1.06E-05	$n_d$	7
$D_w$ (cm <sup>2</sup> s <sup>-1</sup> )	1.28E-06	$\lambda$	21
$K_{darcy}$ (cm <sup>2</sup> )	1.58E-14	$i_{o,an}$ (A cm <sup>-2</sup> )	1.00E-07
$\rho_{H_2O}$ (g cm <sup>-3</sup> )	1	$i_{o,cat}$ (A cm <sup>-2</sup> )	1.00E-01
$\mu_{H_2O}$ (g cm <sup>-1</sup> s <sup>-1</sup> )	1.10E-02	$\alpha_{an}$	0.8
$\epsilon$	0.3	$\alpha_{cat}$	0.25

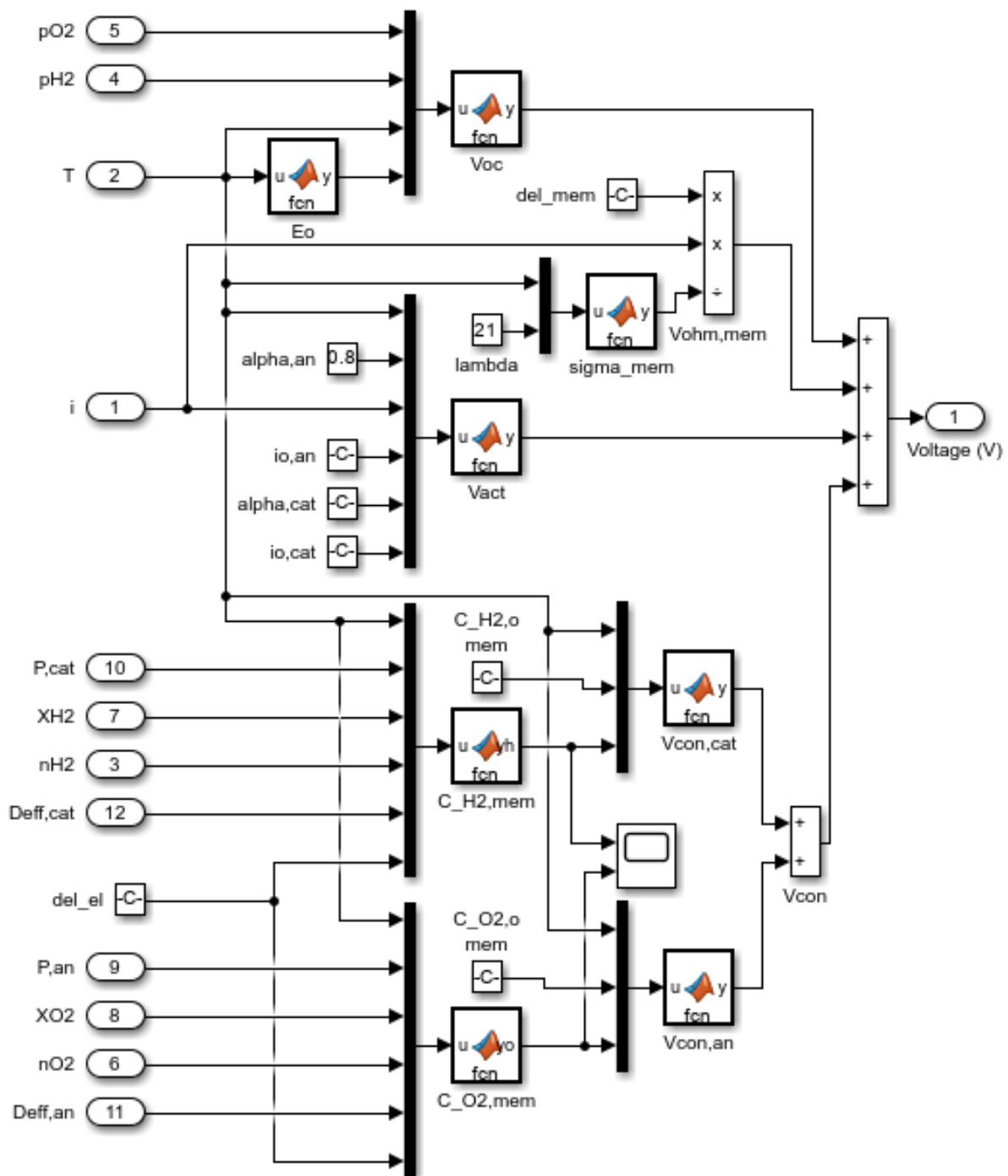


Figure 4.8 Simulink model of the voltage subsystem in the electrolyzer

The electrolyzer model takes power, anode pressure, cathode pressure, temperature as the inputs and gives molar flow rate of hydrogen and oxygen as the output.



### 4.3 Hydrogen Storage Modelling

The hydrogen produced by the electrolyzer needs to be stored in a storage tank. Without a compressor or pump, hydrogen can fill up the tank/cylinder only until the pressure inside the tank reaches the electrolyzer cathode pressure. This report considers a simple scenario of hydrogen storage without accounting for the compression requirements.

As the load and solar radiation vary throughout the day, electrolyzer and fuel cell alternatively switch accordingly. It is important to know whether the amount of hydrogen produced during a day is greater than the amount of hydrogen consumed. It can be obtained as follows

$$\int N_{H_2}^{in} dt - \int N_{H_2}^{out} dt = N_{H_2}^{net} \quad (4.68)$$

Where  $N_{H_2}^{in}$  and  $N_{H_2}^{out}$  are the molar flow rates of hydrogen from the electrolyzer and into the fuel cell respectively,  $N_{H_2}^{net}$  (mol) is the net number of moles remaining in the tank after the given time period.

The volume of the net number of moles remaining is given by the ideal gas equation as

$$Vol_{H_2}^{std} = \frac{N_{H_2}^{net} RT}{P} \quad (4.69)$$

Where  $Vol_{H_2}^{std}$  is volume of hydrogen at standard conditions, T is 273.15 K, P is 1 bar.

The Simulink model of the hydrogen storage tank is shown in Figure 4.9.

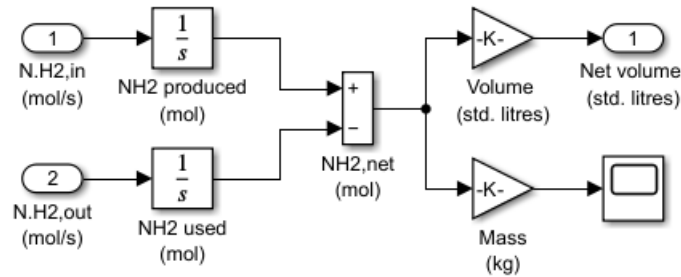


Figure 4.9 Simulink model of the hydrogen storage tank

### 4.4 Fuel Cell Modelling

The power produced from electrolysis depends on multiple factors like fuel cell hydrogen flow rate, oxygen (air) flow rate, electrode area, operating temperature, and pressure. The deficit in renewable energy provided to the load should initiate the fuel cell operation. In the current model, the fuel cell is given an input of how much power is required and the fuel cell runs according to the given conditions to supply the required power. Ideally, the fuel cell should run at 1.23 V, but it cannot run at 1.23 V practically due to multiple losses. These include ohmic overpotential, concentration overpotential, and activation overpotential.

Mathematical modelling of a fuel cell has been done extensively in many ways over the years. Parameters like partial pressure and molar flow rate of hydrogen, and oxygen, current



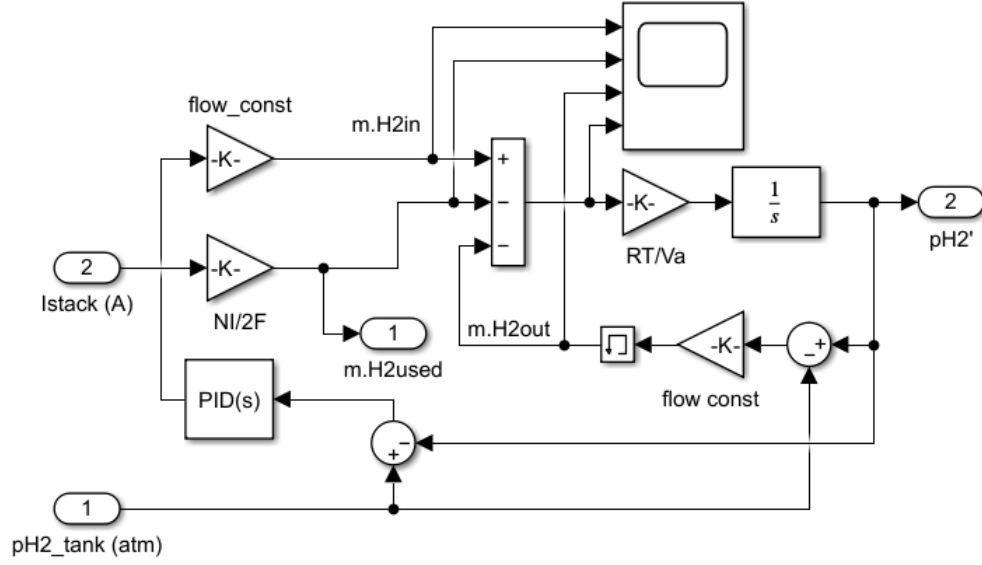


Figure 4.11 Simulink model of the anode H<sub>2</sub> flow subsystem in the fuel cell

#### 4.4.2 Cathode O<sub>2</sub> Flow

The instantaneous reactant pressure for anode is given as

$$\frac{dP'_{O_2}}{dt} = \frac{RT}{V_c} (m_{O_2,in} - m_{O_2,out} - m_{O_2,used}) \quad (4.73)$$

Where  $P'_{O_2}$  is the partial pressure of oxygen,  $V_c$  is volume of cathode,  $m_{O_2,in}$  and  $m_{O_2,out}$  are inlet and outlet molar flow rates of oxygen,  $m_{O_2,used}$  is the rate at which the gas is being used, which can be expressed as

$$m_{O_2,used} = \frac{NI}{4F} \quad (4.74)$$

$m_{O_2,out}$  can be expressed as

$$m_{O_2,out} = k_c (P'_{O_2} - P_{bpr}) \quad (4.75)$$

Where  $k_c$  is the cathode flow constant,  $P_{bpr}$  is the pressure pre-defined by the back-pressure regulator.  $m_{O_2,in}$  is evaluated as the product of air (oxygen) flow rate with the oxygen mole fraction in air (21% for normal terrain).

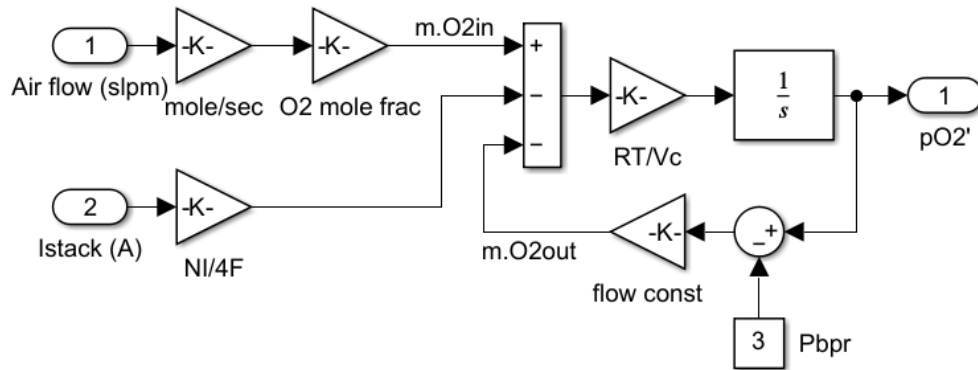


Figure 4.12 Simulink model of the cathode O<sub>2</sub> flow subsystem in the fuel cell

#### 4.4.3 Fuel Cell

The output voltage can be expressed as the algebraic sum of the thermodynamic (Nernst), activation, ohmic and concentration overpotentials.

$$V_{cell} = E_{Nernst} + \eta_{act} + \eta_{ohm} + \eta_{con} \quad (4.76)$$

The stack voltage is given as

$$V_{stack} = NV_{cell} \quad (4.77)$$

The thermodynamic potential is given by the Nernst equation as

$$E_{Nernst} = E_o + \frac{RT}{nF} \left( \ln(p'_{H2} \sqrt{p'_{O2}}) \right) \quad (4.78)$$

Where  $E_o$  is the reference thermodynamic potential, given as

$$E_o = 1.229 - 0.85 * 10^{-3} (T - 298) \quad (4.79)$$

The activation overpotential can be expressed by the following empirical relation

$$\eta_{act} = \xi_1 + \xi_2 T + \xi_3 T (\ln(c'_{O2})) + \xi_4 T (\ln(I)) \quad (4.80)$$

Where  $\xi_i$  are parametric coefficients,  $c'_{O2}$  is the  $O_2$  concentration at the membrane-cathode interface. The parametric coefficients are given as

$$\xi_1 = -0.948 \quad (4.81)$$

$$\xi_2 = 0.00286 + 0.0002 \ln(A) + 4.3 * 10^{-5} \ln(c'_{H2}) \quad (4.82)$$

$$\xi_3 = 7.6 * 10^{-5} \quad (4.83)$$

$$\xi_4 = -1.93 * 10^{-4} \quad (4.84)$$

Where A is the cell area,  $c'_{H2}$  is the  $H_2$  concentration at the membrane-anode interface. These concentrations are determined by Henry's law as

$$c'_{O2} = p'_{O2} * 1.97 * 10^{-7} \exp\left(\frac{498}{T}\right) \quad (4.85)$$

$$c'_{H2} = p'_{H2} * 9.174 * 10^{-7} \exp\left(\frac{-77}{T}\right) \quad (4.86)$$

To incorporate the effect of double layer capacitance, the activation overpotential is further modified as follows, incorporating a feedback loop for the activation overpotential.

$$V_{act} = -\eta_{act} \quad (4.87)$$

$$R_{act} = \frac{V_{act}}{I} \quad (4.88)$$

$$\frac{dV_{act}}{dt} = \frac{I}{C_{dl}} - \frac{V_{act}}{R_{act} C_{dl}} \quad (4.89)$$

For the ohmic overpotential, the membrane's resistance to conduction of protons is the most significant factor. It is given as

$$\eta_{ohm} = -iR_{int} \quad (4.90)$$

Where  $R_{int}$  is the internal resistance of the membrane. It can be expressed in terms of membrane resistivity,  $r_M$  given as

$$R_{int} = \frac{r_M l_{mem}}{A} \quad (4.91)$$

Where  $l_{mem}$  is the thickness of the membrane. Membrane resistivity can be expressed by the following empirical relation

$$r_M = \frac{181.6 \left( 1 + 0.03 \left( \frac{l}{A} \right) + 0.062 \left( \frac{T}{303} \right)^2 \left( \frac{l}{A} \right)^{2.5} \right)}{\left( \lambda - 0.634 - 3 \left( \frac{l}{A} \right) \right) \exp \left( 4.18 \left( \frac{T - 303}{T} \right) \right)} \quad (4.92)$$

Where  $\lambda$  is the membrane resistivity parameter, dependent on factors like stoichiometric anode inlet gas ratio, humidity of membrane.

The concentration overpotential is given as [20]

$$\eta_{con} = N * m \exp \left( \frac{nl}{A} \right) \quad (4.93)$$

Where  $m$  and  $n$  are constants in the mass transfer voltage.

Evaluating Eq. (4.70) to Eq. (4.93) gives the output voltage of the fuel cell. The stack current is obtained from the input of power required and output voltage through a feedback loop. The fuel cell model takes power required, H<sub>2</sub> tank pressure, air flow rate, temperature as the inputs and gives stack current and stack voltage as the output. The gas coming from H<sub>2</sub> tank is regulated at a constant pressure of 3 atm by a pressure regulator.

Values of parameters used in this model are given in Table 4.3.

Table 4.3 Parameters used in the fuel cell model [15]

Parameter	Value	Parameter	Value
N	35	F (C mol <sup>-1</sup> )	96485
A (cm <sup>2</sup> )	232	C <sub>dl</sub> (F)	8.12
l <sub>mem</sub> (cm)	0.0178	λ	12.5
P <sub>tank</sub> (atm)	3	V <sub>a</sub> (m <sup>3</sup> )	0.005
P <sub>bpr</sub> (atm)	3	k <sub>a</sub> (mol s <sup>-1</sup> atm <sup>-1</sup> )	0.065
Rated Power (kW)	5	V <sub>c</sub> (m <sup>3</sup> )	0.01
R (J mole <sup>-1</sup> K <sup>-1</sup> )	8.314	k <sub>c</sub> (mol s <sup>-1</sup> atm <sup>-1</sup> )	0.065

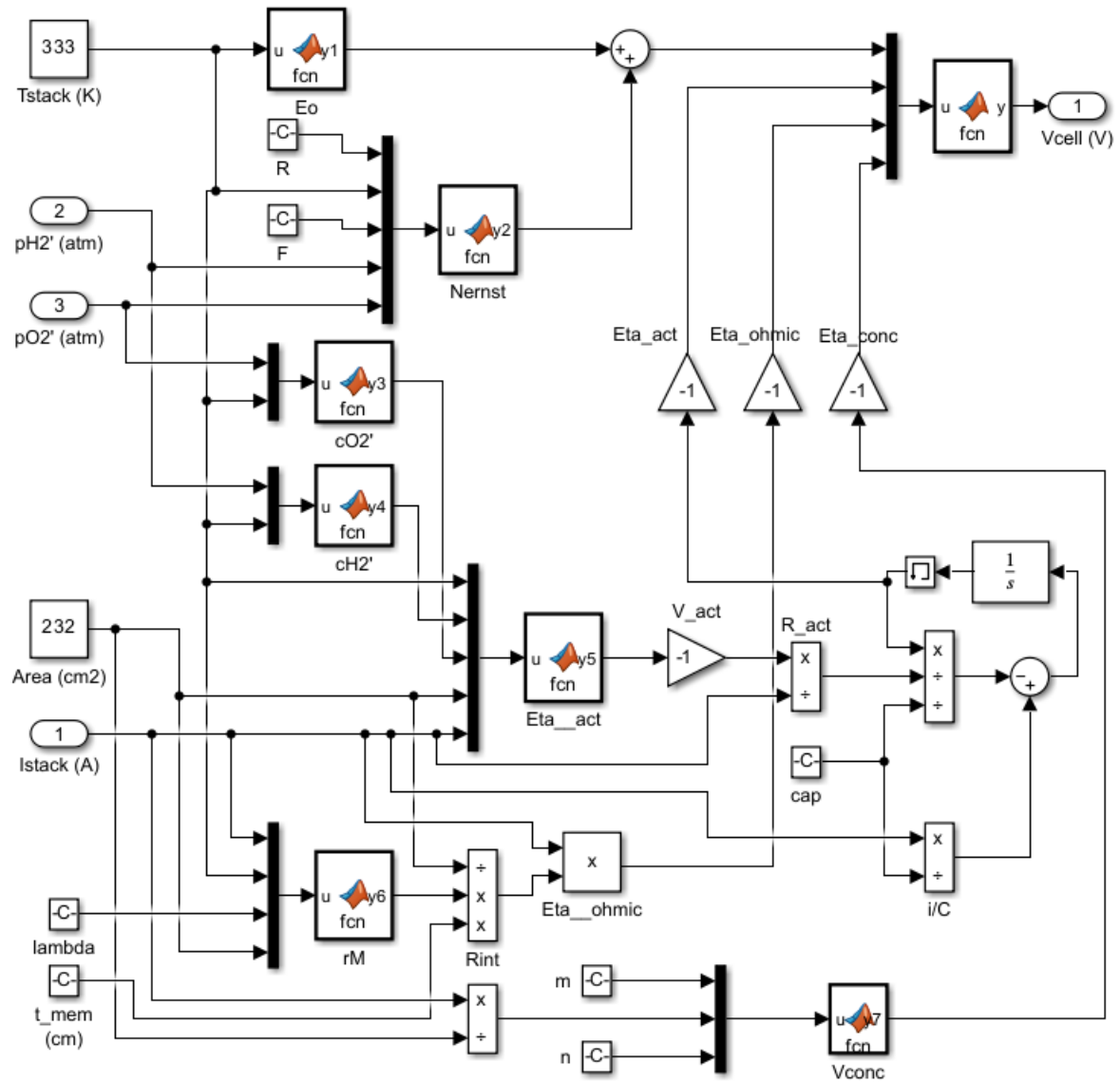


Figure 4.13 Simulink model of the fuel cell subsystem in the fuel cell

#### 4.5 Passive Solar Tent Modelling

Design of a passive heating system involves selection and sizing of the passive feature types and determination of thermal performance. The method followed here gives an estimate of the auxiliary heating requirement,  $Q_{aux}$ , for a system. Figure 4.14 shows the flow of calculations to estimate the  $Q_{aux}$  for a particular design. [10]

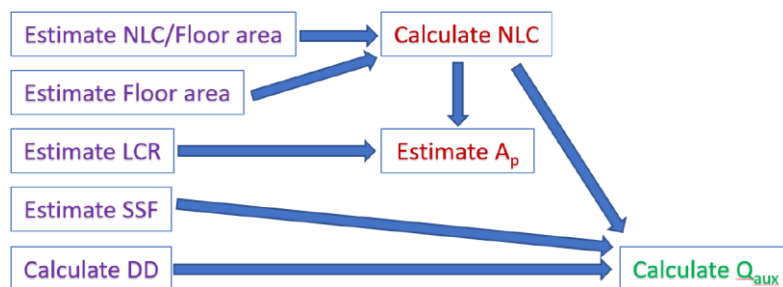


Figure 4.14 Flowchart of calculations to estimate auxiliary heating requirement

#### 4.5.1 Net Load Coefficient

A design heating load of 120-160 kJ/C-day-m<sup>2</sup> is considered an energy-conservative design in conventional building design. These non-solar values are reduced by 20% to consider the solarization of the south-facing wall, giving a rule-of-thumb heating load of 100-130 kJ/C-day-m<sup>2</sup>. Average value of 115 kJ/C-day-m<sup>2</sup> is taken for calculations in this project. It should be noted that the area quantity in the denominator is floor area, and C-day refers to Degree Days in Celsius. This quantity is known as the Net building Load Coefficient (*NLC*) per unit floor area. Thus, it can also be understood as energy per Degree Day per m<sup>2</sup> of floor area. [10]

#### 4.5.2 Degree Days

The effect of the outdoor temperature on the heating load is estimated in terms of Degree Days. Heating Degree Days (*DD*) is the sum of the differences between a fixed base temperature and the daily mean temperatures (only positive differences are counted, that is, when the outdoor mean is less than the base temperature). The daily mean temperatures are computed as the means of the daily minimum and maximum temperatures. The base temperature could be understood such that when the indoor temperature goes lower than the base temperature, indoor heating needs to be done. [10]

The base temperature in the definition of *DD* is taken as 10° C for Ladakh. Hence Degree Days can be calculated as:

$$DD = \left( T_{base} - \frac{T_{max} + T_{min}}{2} \right) (No. of days) \quad (4.94)$$

For the Leh region in Ladakh, data on daily temperatures over a year was not available. Hence, the monthly data of minimum and maximum temperatures of Leh was used. [16] Calculations to obtain the Degree Days number are shown in Figure 4.15. Final number of Degree Days for a year in Leh is 2896 C-Days (Celsius Days).

Month	Min T in F	Min T in C	Max T in F	Max T in C	Days	Days*Mean T (C-days)	Days*Base T	Difference	Degree Days
January	4	-15.6	26	-3.3	31	-292.8	310	602.8	2896
February	5	-15.0	28	-2.2	28	-241.1	280	521.1	
March	14	-10.0	36	2.2	31	-120.6	310	430.6	
April	27	-2.8	47	8.3	30	83.3	300	216.7	
May	35	1.7	56	13.3	31	232.5	310	77.5	
June	41	5.0	66	18.9	30	358.3	300	-58.3	
July	47	8.3	74	23.3	31	490.8	310	-180.8	
August	46	7.8	73	22.8	31	473.6	310	-163.6	
September	38	3.3	64	17.8	30	316.7	300	-16.7	
October	29	-1.7	49	9.4	31	120.6	310	189.4	
November	19	-7.2	39	3.9	30	-50.0	300	350.0	
December	10	-12.2	31	-0.6	31	-198.1	310	508.1	

Figure 4.15 Calculation of Degree Days for Leh

#### 4.5.3 Solar Savings Fraction

Solar Savings Fraction (*SSF*) is the fractional reduction in required auxiliary heating relative to net reference load (building load,  $Q_{net}$ , taken as *NLC* here based on the nature of calculations). *SSF* cannot be viewed as a measure for comparing two solar buildings. Such a comparison is valid only if both the buildings have the same *NLC*. Instead, the auxiliary heat

requirement,  $Q_{aux}$ , is a valid performance measure.  $Q_{aux}$  is the conventional heat delivered to the building to supplement solar heat. [10]

$$SSF = 1 - \frac{Q_{aux}}{Q_{net}} \quad (4.95)$$

Based on the estimation of  $SSF$  by various sources for various regions,  $SSF$  for the Ladakh region is taken as 0.75.

#### 4.5.4 Auxiliary Heat

Now, there are estimates for  $NLC/floor\ area$ ,  $DD$ , and  $SSF$ .  $NLC$  can be obtained by multiplying it with the estimated floor area. Finally, auxiliary heat,  $Q_{aux}$ , can be calculated from  $NLC$ ,  $SSF$ , and  $DD$  as

$$Q_{aux} = (1 - SSF) Q_{net} = (1 - SSF) * NLC * DD \quad (4.96)$$

The floor area for the considered solar tent is calculated as length\*breadth of north/south-facing wall and east/west-facing wall respectively.

$$NLC = \left( \frac{NLC}{Floor\ Area} \right) * Floor\ Area \quad (4.97)$$

Substituting Eq. (4.96) in Eq. (4.95) gives

$$Q_{aux} = (1 - SSF) * \left( \frac{NLC}{Floor\ Area} \right) * Floor\ Area * DD \quad (4.98)$$

In Eq. (4.97),  $SSF$ ,  $(NLC/Floor\ Area)$ ,  $DD$  have been estimated in the above subsections. Hence, the auxiliary heat requirement can be calculated with an estimate of the floor area of the tent. [10]

#### 4.6 Overall System Model

Integration of solar PV array, electrolyzer, hydrogen storage tank, and fuel cell has been done in this model. The system is designed for a 2-kW capacity. The rated power of solar panels is 400 W. Hence, the number of solar panels has been chosen as 5, connected in series. The electrolyzer performs very well in the range of 400-500 W. The number of electrolyzers has been chosen to be up to 5 based on input conditions. The fuel cell is capable of performing well even beyond 2 kW. Hence, the number of fuel cell stacks is 1.

The solar PV system takes input of temperature and irradiance. The lower input irradiance is limited at 100 W to incorporate the real-life scenario of a solar panel producing electricity only with a sufficient amount of irradiance. The power generated from the solar array goes to load first. When the load's requirements are fulfilled, the remaining power is diverted towards the electrolyzer.

The electrolyzer system takes in the remaining power and based on the range of input power, the number of electrolyzers are activated. For 0-400 W, one electrolyzer is active. For 401-800 W, two electrolyzers are active. For 801-1200 W, three electrolyzers are active. For 1201-1600 W, four electrolyzers are active. For 1600+ W, all five electrolyzers are active. When the load requirement is more than the power that solar array can supply, the electrolyzer



remains in non-operational state. The output of this system is the molar flow rate of hydrogen and oxygen, which head towards the hydrogen storage.

The fuel cell system gets activated when the power supplied to the load by the solar array is lesser than the requirement. When the solar array is sufficient to power the load, fuel cell remains in non-operational state. This deficit of power is given as input for fuel cell, which operates at the given conditions of pressure, flow rate and temperature by using hydrogen from hydrogen storage and hence producing the required power.

The hydrogen storage system takes input of the molar flow rate of hydrogen coming in from the electrolyzer and the molar flow rate of hydrogen required by the fuel cell during operation. It outputs the net volume of hydrogen remaining after the time period of operation. The output is in standard litres. The effect of tank pressure can be included by dividing the number of standard litres by the tank pressure in bar.

The efficiency of solar PV is calculated by considering the input irradiance, the rated power of a panel, and its area. The efficiency of electrolyzer is calculated by considering the input power, the molar flow rate of the output hydrogen, and the higher heating value of hydrogen (since all operating temperatures are below the boiling point of water). The efficiency of fuel cell is calculated by considering the molar flow rate of the hydrogen used, the output power, and the heating value of hydrogen.

Heat is also generated due to the inefficiencies of electrolyzer and fuel cell. For electrolyzer, the difference between the input power and the product of output molar flow rate and HHV of hydrogen is calculated as the heat released, in terms of power. For fuel cell, the difference between the product of used molar flow rate and HHV of hydrogen, and the output power is calculated as the heat released during operation.

This heat, along with the ancillary systems fulfil the heating load. The power requirement for ancillary systems is fulfilled through the power output of solar array and fuel cell, when operational.

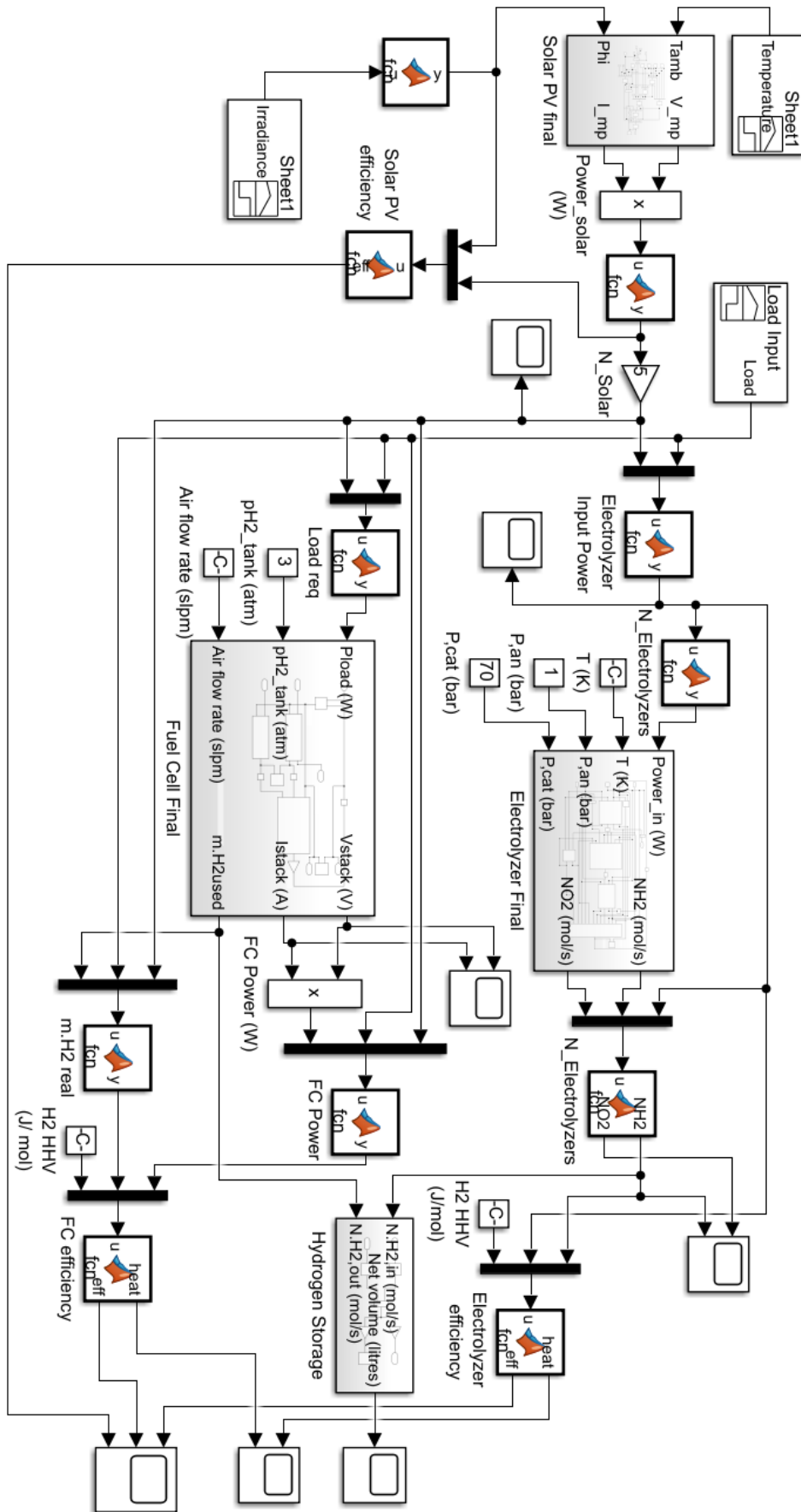


Figure 4.16 Simulink model of entire solar hydrogen system

## 5. Results and Discussion

A comprehensive analysis was conducted on all the individual systems comprising the solar PV array, electrolyzer, fuel cell, and solar tent. Each system was assessed under standard working conditions specific to their respective functionalities. The obtained results from these analyses are presented in this chapter, providing valuable insights into the performance and efficiency of each system component. By examining the data gathered under controlled conditions, a deeper understanding of the overall system's capabilities and limitations can be achieved, enabling informed discussions on its practical implementation and potential for sustainable energy utilization.

### 5.1 Passive Solar Tent

The passive solar tent being considered for this project is a semi-cylindrical-roof tent, as explained in Subsection 3.5.2. The dimensions of the tent are as follows – 9 m in length (north/south-facing wall), 5 m in breadth (east/west-facing wall), 2.5 m in height, as shown in Figure 5.1.

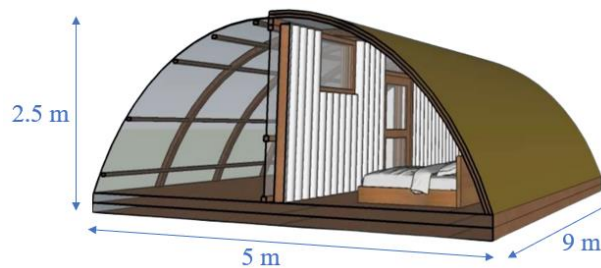


Figure 5.1 Dimensions of the passive solar tent [13]

The floor area is  $9 \text{ m} \times 5 \text{ m} = 45 \text{ m}^2$ . Substituting the value of floor area in Eq. (4.97) along with other pre-determined parameters gives the value of  $Q_{aux}$  as 3747.7 MJ per year or about 1041 kWh per year.

This is the energy required annually by the auxiliary heating devices, i.e., the active space heating systems, which also account for the heating requirements of days with little or no sun. To fulfil this heating load, the locals in Ladakh burn firewood and kerosene and use electric room heaters.

### 5.2 Solar PV

Ladakh benefits from an average solar irradiation of  $5.5 \text{ kWh/m}^2\text{-day}$ , coupled with approximately 300 sunny days annually. Leveraging this abundant solar resource, a 1 kW solar PV array has the potential to generate 1650 kWh of clean energy per year. With a larger 2 kW system implemented in this project, an estimated annual energy production of 3300 kWh can be achieved. Remarkably, this output surpasses the auxiliary heat requirement of the solar tent by threefold. Factoring in the efficiencies of the various components, this system not only fulfils the heating needs of the tent but also has the capability to power additional loads.

The solar PV model was tested under various operating conditions and the results are presented here. At STC (cell temperature of 25 °C, irradiance of 1000 W/m<sup>2</sup>), the model outputs  $V_{mp}$  of 40.42 V and  $I_{mp}$  of 9.9 A. From the IV curve obtained, as shown in Figure 5.2, the  $V_{oc}$  and  $I_{sc}$  are 49.28 V and 10.2 A respectively. These values match very closely to the manufacturer's rated values, validating the model at Standard Test Conditions.

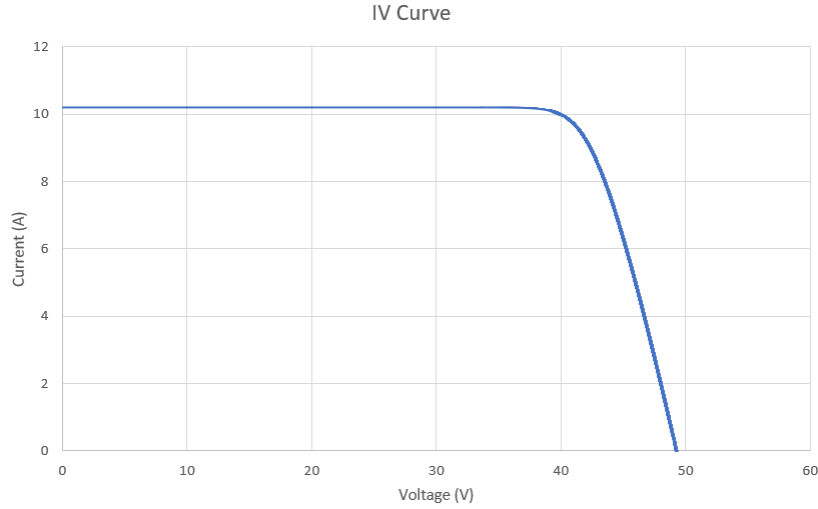


Figure 5.2 IV curve of solar model under STC

The model has been tested at different irradiances ranging from 500 W/m<sup>2</sup> to 1100 W/m<sup>2</sup>. The ambient temperature input was set to 269.25 K and the cell temperature varies with the input irradiance according to the Eq. (4.16). The results are shown in Figure 5.3. The short circuit current  $I_{sc}$  varies considerably with change in irradiance, while the open circuit voltage,  $V_{oc}$ , varies only slightly with irradiance. This observed behaviour aligns with expectations, as the impact of irradiance on the current should be significantly more pronounced than on the voltage.

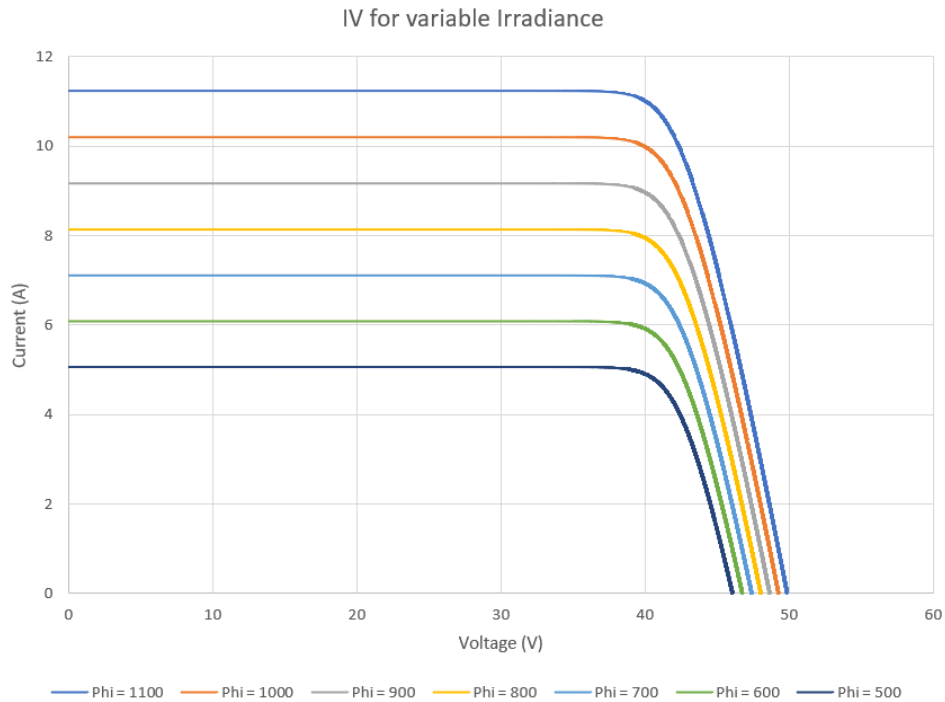


Figure 5.3 IV curve of solar model under variable irradiance

The model was subjected to further rigorous testing across a continuous range of irradiance from  $100 \text{ W/m}^2$  to  $1100 \text{ W/m}^2$ . The ambient temperature input was set to  $269.25 \text{ K}$ , like the previous test. The output power vs irradiance plot is shown in Figure 5.4. Power increases linearly with irradiance at constant temperature. There are no deviations and this aligns with the expectations.

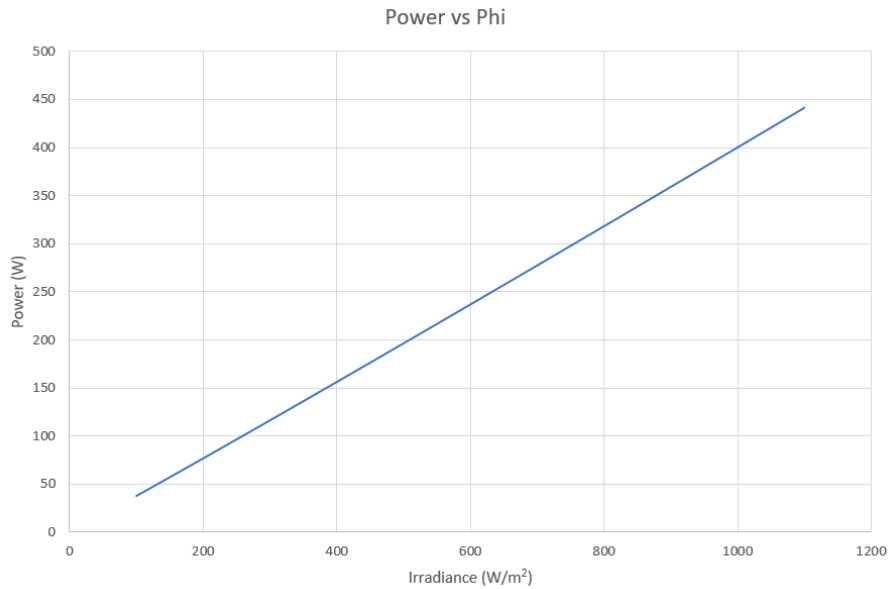


Figure 5.4 Variation of output power with irradiance at constant temperature

The obtained results from the three conducted tests consistently align with our initial expectations, thereby providing strong validation for the developed model under variable conditions.

### 5.3 Electrolyzer

The electrolyzer has been modelled such that the final output is voltage, which depends on the input power, pressure of anode and cathode, cell temperature among other internal parameters of the electrolyzer. The model has been tested at a cathode pressure of 70 bar, anode pressure of 1 bar, and cell temperature of  $313 \text{ K}$ . To obtain the polarization curve, the input power has been varied from about  $10 \text{ W}$  to  $440 \text{ W}$ . The polarization curve is shown in Figure 5.5.

For very low current densities, the electrolyzer model was getting initiated and it took some time for the system to function as expected. The steep rise for current density less than  $0.14 \text{ A/cm}^2$  can be attributed to activation overpotential. The steady and linear-like rise from  $0.15 \text{ A/cm}^2$  to about  $1.2 \text{ A/cm}^2$  is due to the contribution of ohmic overpotential. Hence, from this graph it is shown that activation overpotential dominates in lower current density region, while ohmic overpotential dominates in the medium current density region. The third overpotential, the concentration or mass-transfer overpotential dominates in the higher current density regions, for current densities greater than  $1.5\text{--}2 \text{ A/cm}^2$ . But electrolyzers are generally not operated at such high current densities as they lead to many losses. This curve matches closely with the polarization curve given in [14]

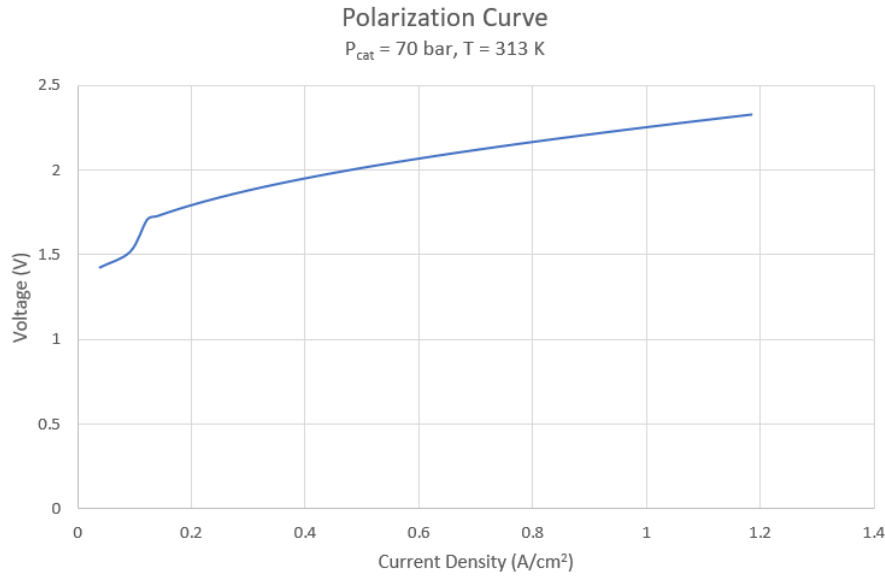


Figure 5.5 Polarization curve of electrolyzer

Figure 5.6 shows the contribution of each of the overpotentials to the operating voltage. Initial few values of negative voltage have been omitted, which were due to the initialization of parameters during the early cycles in the developed model. The contribution of  $V_{oc}$ , attributed to the Nernst equation, remains relatively constant, aligning with our expectations. Among the overpotentials, activation overpotential emerges as the most influential. Its magnitude is notably higher at lower current densities and exhibits a steady increase as the current density rises. In contrast, ohmic overpotential exhibits a proportional relationship with current density, starting from lower values and displaying a linear growth pattern. Concentration overpotential, on the other hand, demonstrates minimal significance at lower or normal current densities. Although it gradually increases with current density, it remains relatively small within the operational range of current densities.

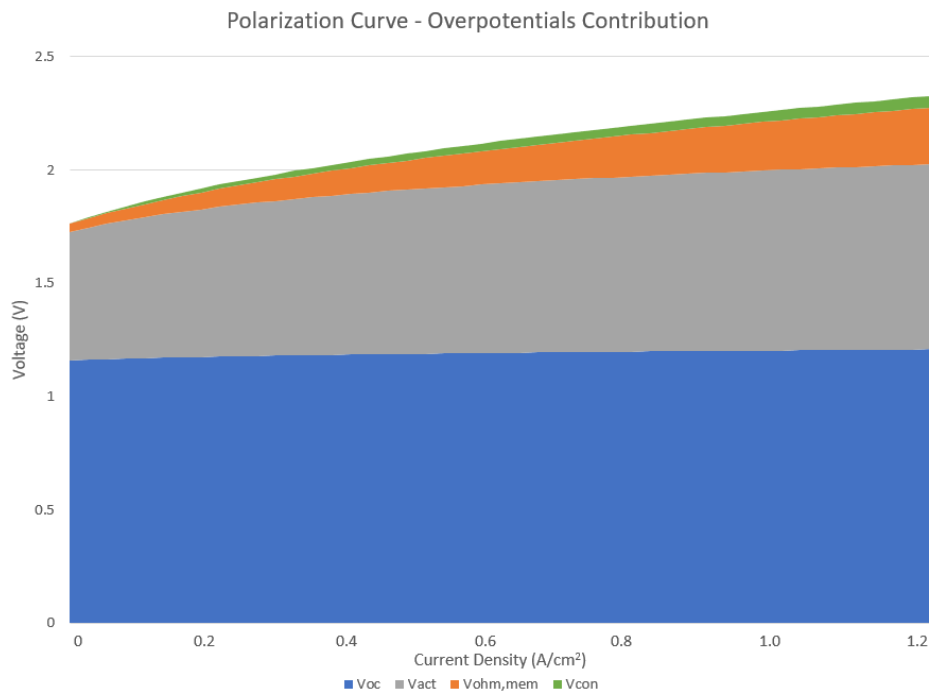


Figure 5.6 Contribution of different overpotentials to the operating voltage of electrolyzer

## 5.4 Fuel Cell

The fuel cell has been modelled such that the final output is voltage and current, which depend on the power deficit on load side, pressure of hydrogen gas from tank and air (oxygen) flow rate, stack temperature among other internal parameters of the fuel cell. The model has been tested at hydrogen pressure of 3 atm, air flow rate of 150 slpm, and stack temperature of 333 K. To obtain the polarization curve, the power required (same as power output) has been varied from 3 W to 3000 W. The polarization curve is shown in Figure 5.7.

The steep fall for current density less than  $0.2 \text{ A/cm}^2$  can be attributed to activation overpotential. The steady and linear-like all from  $0.25 \text{ A/cm}^2$  to about  $0.8 \text{ A/cm}^2$  is due to the contribution of ohmic overpotential. Hence, from this graph it is shown that activation overpotential dominates in lower current density region, while ohmic overpotential dominates in the medium current density region. The third overpotential, the concentration or mass-transfer overpotential dominates in the higher current density regions, for current densities greater than  $1.5\text{--}2 \text{ A/cm}^2$ . But fuel cells are generally not operated at such high current densities as they lead to many losses. This curve matches closely with the polarization curve given in [15]

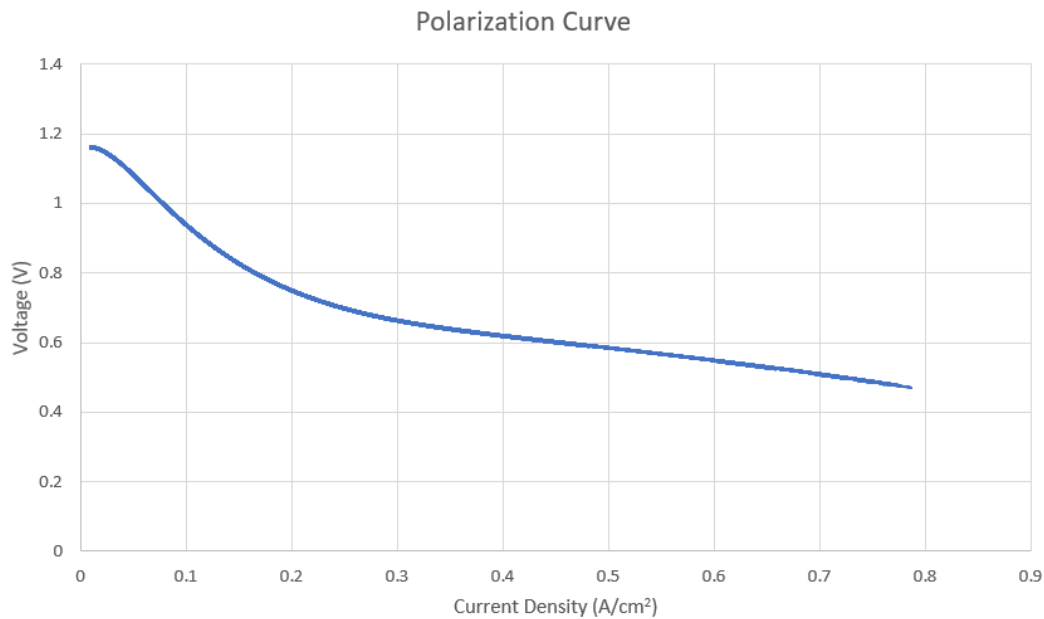


Figure 5.7 Polarization curve of fuel cell

Figure 5.8 shows the contribution of each of the overpotentials to the operating voltage. The contribution of  $V_{oc}$ , attributed to the Nernst equation, remains relatively constant, aligning with our expectations. The effect of other overpotentials is negative on the overall voltage. Only the thermodynamic voltage,  $V_{oc}$  is positive. Among the overpotentials, activation overpotential emerges as the most influential. Its magnitude increases steeply at lower current densities and exhibits a steady increase as the current density rises. In contrast, ohmic overpotential exhibits a proportional relationship with current density, starting from lower values and displaying a linear growth. Concentration overpotential, on the other hand, demonstrates minimal significance at lower or normal current densities. Although it gradually increases with current density, it remains relatively very small within the operational range of current densities.

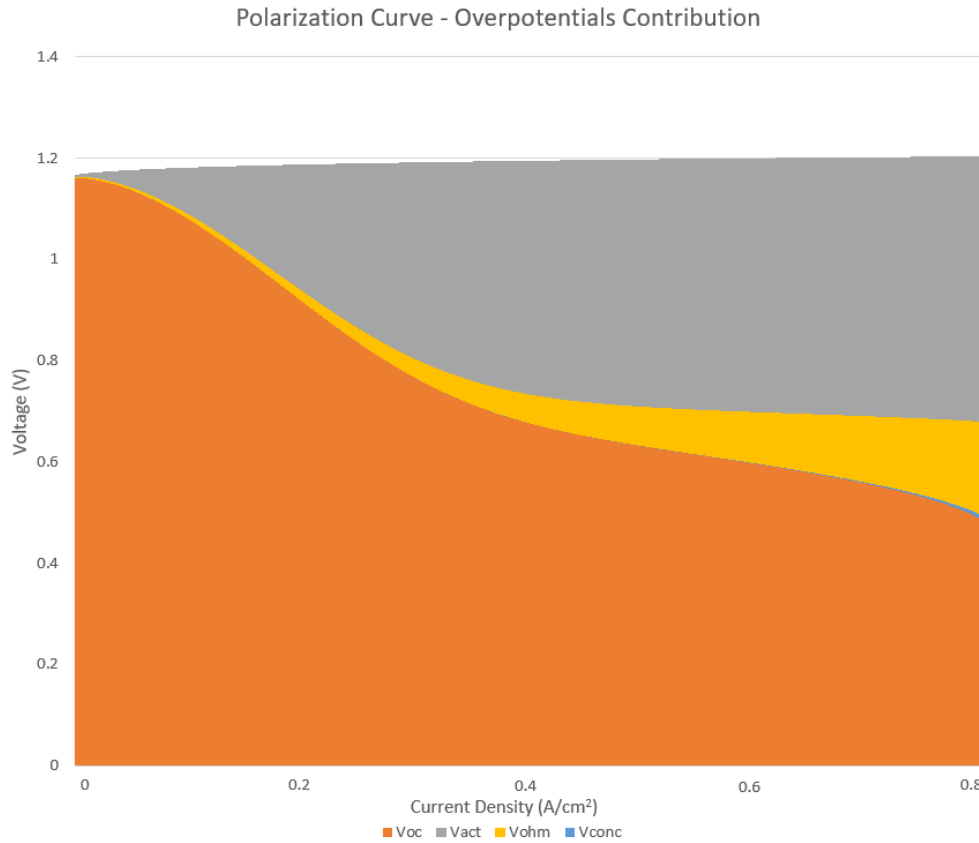


Figure 5.8 Contribution of different overpotentials to the operating voltage of fuel cell

## 5.5 Overall Model

The simulations conducted on each system individually yielded satisfactory results. The combination of all the systems is also tested under various conditions. The inputs for the overall model are the ambient temperature, irradiance, and load. The results are obtained for three types of loads: no load, constant load (400 W) and variable load (daily profile load).

The temperature and irradiance data are obtained from NSRDB by NREL [17]. Leh has been chosen as the location for the same. The data is obtained for the summer solstice, 21 June, in Leh. It provides the highest input of solar energy in a day in a particular year. This helps in understanding the limits of the system being designed.

The irradiance curve is shown in Figure 5.9. The sunlight starts at 5 am and peaks at 12 noon, with the peak irradiance value almost touching  $1100 \text{ W/m}^2$ . The irradiance reaches zero again at 7 pm, leading to a total of 14 sunshine hours. The total irradiation amounts to  $9.22 \text{ kWh/m}^2\text{-day}$  on this day.

The temperature curve is shown in Figure 5.10. The lowest temperature is at around sunrise time, at  $276.7 \text{ K}$  and the highest temperature is around 1 pm, at  $286.2 \text{ K}$ . The temperature steadily increases from sunrise to noon and slowly falls towards the night.



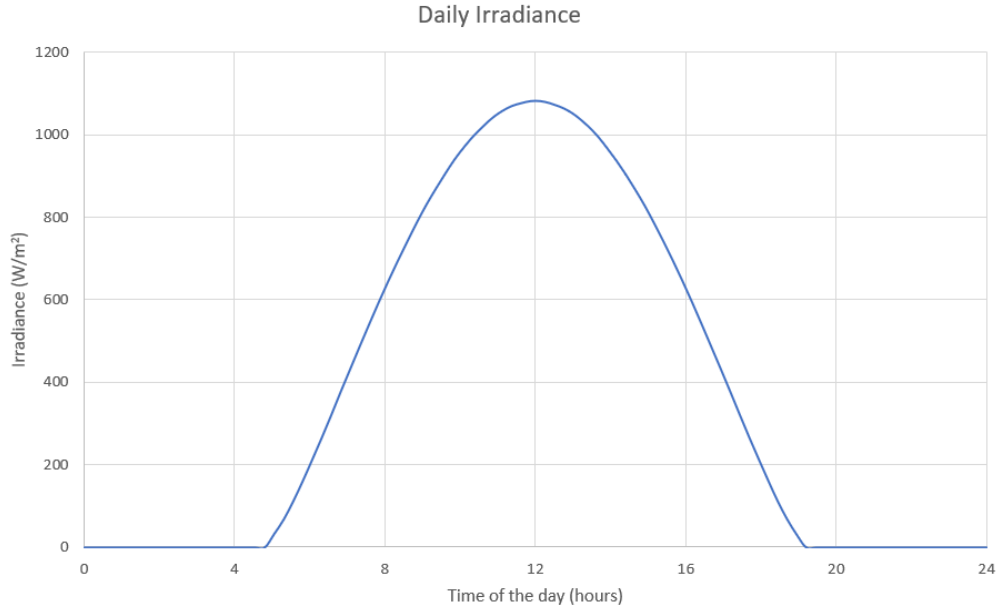


Figure 5.9 Daily irradiance variation in Leh on 21 June

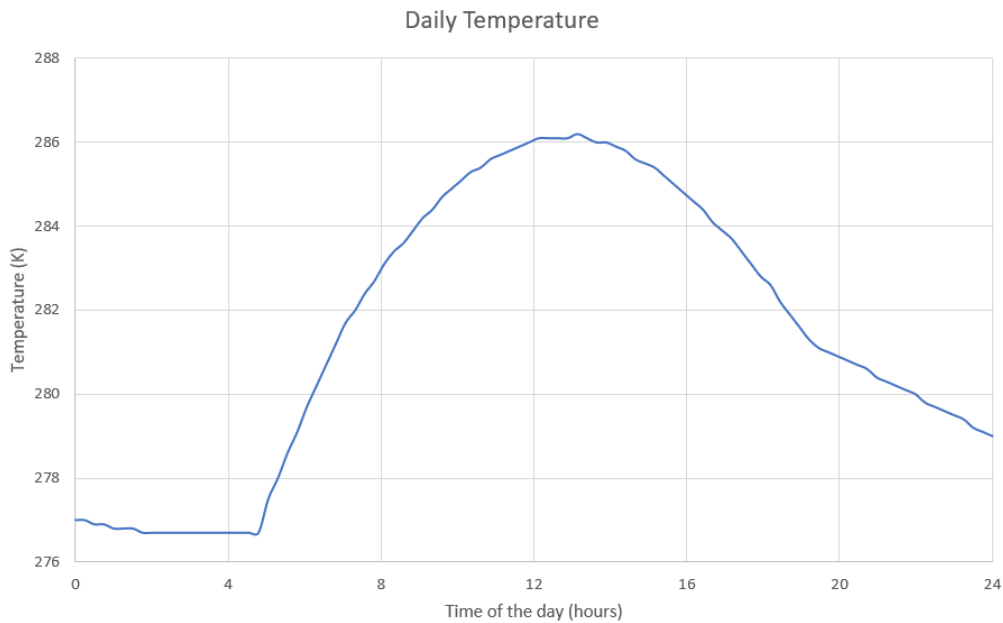


Figure 5.10 Daily temperature variation in Leh on 21 June

Figure 5.11 presents the output of the solar PV array. The observed behaviour demonstrates a remarkable alignment between the solar irradiance and the corresponding electrical output. The two distinct steps observed at the beginning and end of the curve are intentionally incorporated constraints. These constraints have been implemented to prevent any output from being generated when the input solar irradiance falls below  $100 \text{ W/m}^2$ . By incorporating these intentional constraints, the model ensures that output is only produced when the solar irradiance exceeds the specified threshold, effectively capturing the desired operational behaviour of the solar PV array. This output is same for all the load conditions discussed further in the report. The total solar energy output in the day amounts to 19.61 kWh.

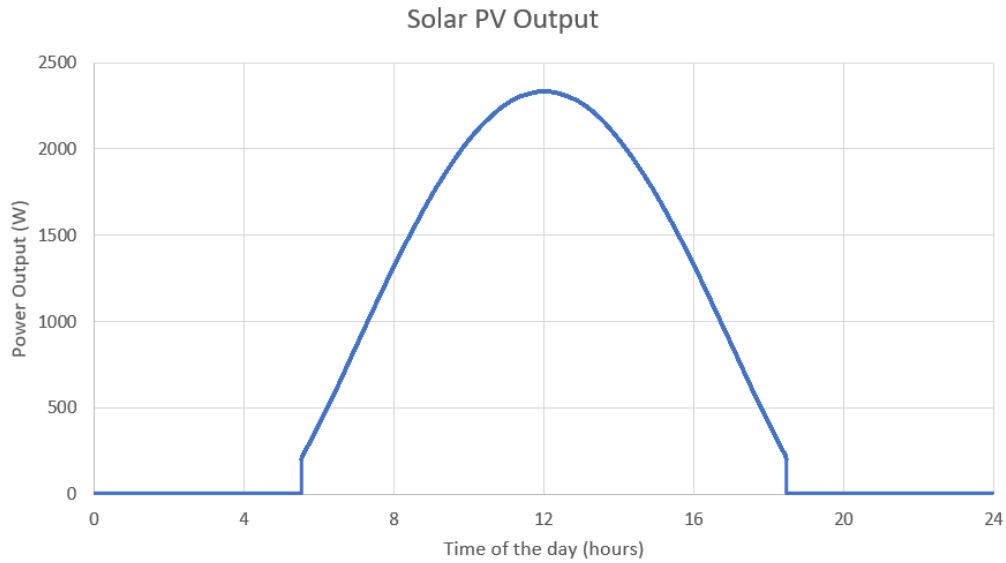


Figure 5.11 Power output of solar PV array

### 5.5.1 Variable Load

Figure 5.12 illustrates the daily load profile employed for the variable load scenario. This profile was custom-generated by taking into account the typical load patterns of a household, while also incorporating additional considerations specific to the current project. Consequently, the load profile exhibits distinct characteristics. Notably, it features a small peak in the morning at 8 am, followed by a decline to near-zero levels during the afternoon hours. Subsequently, the load gradually increases, reaching its maximum value in the evening around 8-9 pm. This combination of factors results in a dynamic load pattern that accurately reflects the energy consumption patterns expected in the given context.

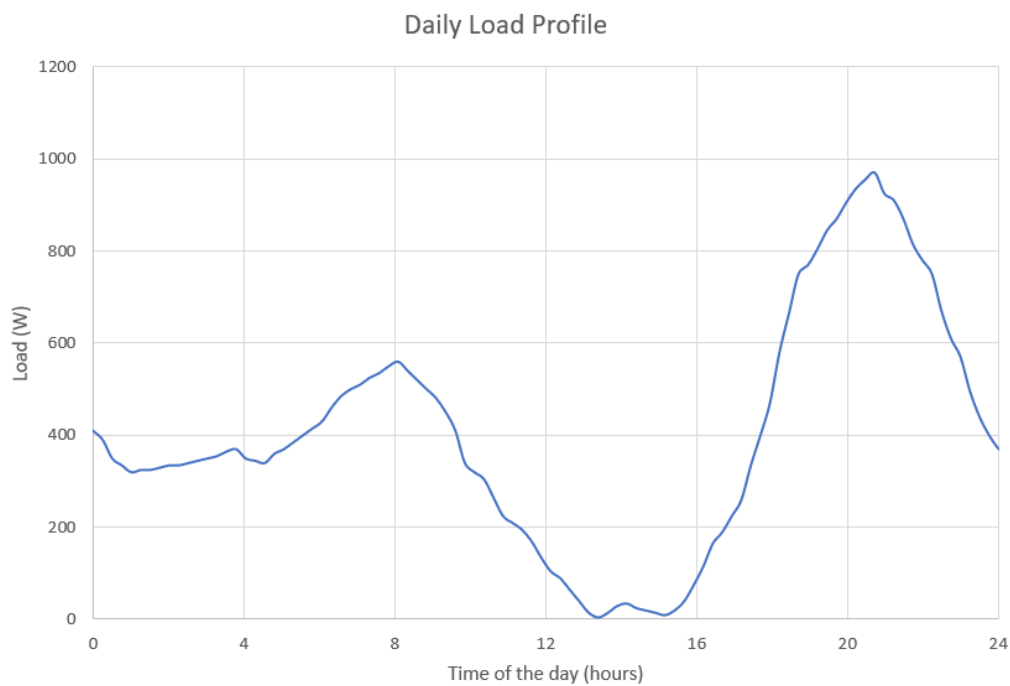


Figure 5.12 Daily load profile for variable load

Figure 5.13 showcases the electrolyzer output for the variable load scenario. The electrolyzer operation begins when the solar array output exceeds the load requirement, starting at around 6:30 am and ending around 6 pm. Notably, the electrolyzer output reaches its peak during the afternoon, when the load is minimal and the solar power output is at its maximum. The curve closely follows the solar output curve, while also being slightly skewed, indicating the non-uniformity of the load distribution about noon. Importantly, the molar flow rate of oxygen consistently maintains a value precisely half that of the molar flow rate of hydrogen at each data point, corroborating the theoretical expectations. It is worth noting that the electrolyzer ceases operation in the absence of sunlight or when the load surpasses the solar output. The maximum observed molar flow rate of hydrogen reaches approximately 0.005 mol/s, highlighting the peak hydrogen production of the electrolyzer within the operating conditions of the system.

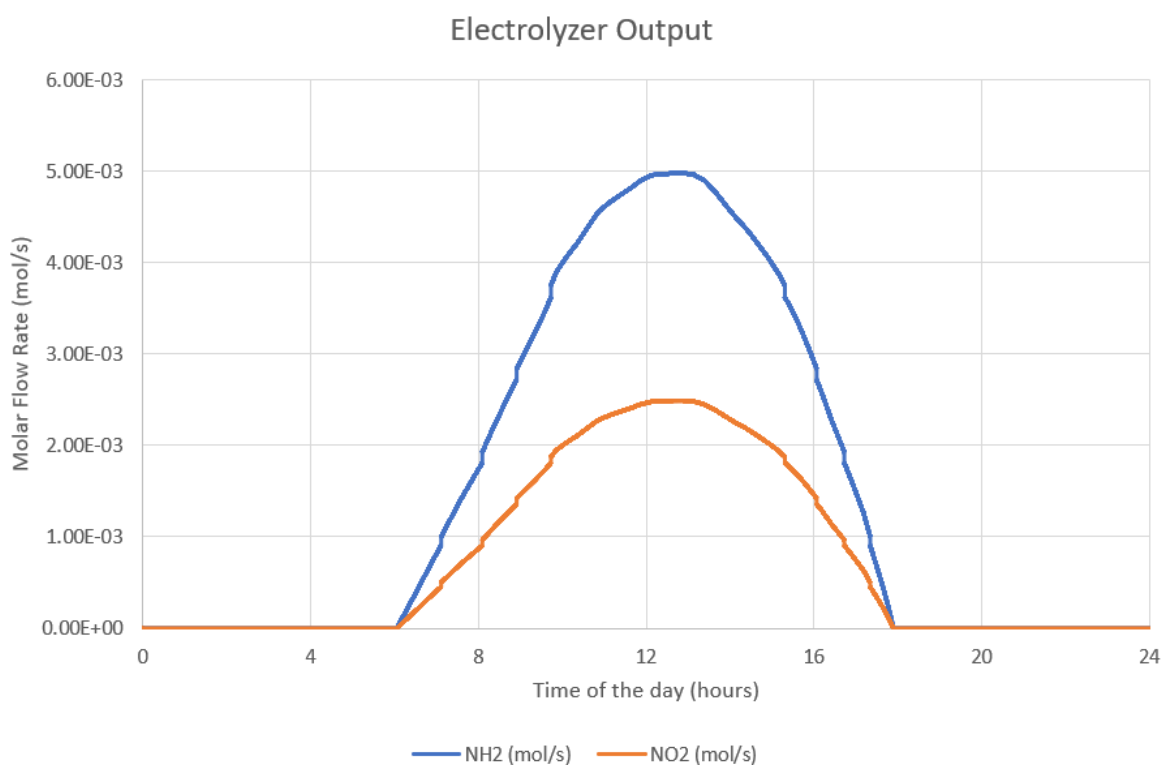


Figure 5.13 Gas molar flow rate output of electrolyzer under variable load conditions

Figure 5.14 illustrates the power output of the fuel cell for the variable load scenario. The fuel cell operation begins when the load requirement exceeds the solar array output, starting at around 6 pm and ending around 6:30 am. Notably, the fuel cell output reaches its peak during the night, when the load is at peak and the solar power output is at zero. The curve closely follows the load profile curve during non-sunshine hours. It is worth noting that the fuel cell ceases operation in the presence of sunlight when the solar output surpasses the load. The maximum observed power output reaches 965 W, highlighting the peak power output of the fuel cell within the operating conditions of the system.

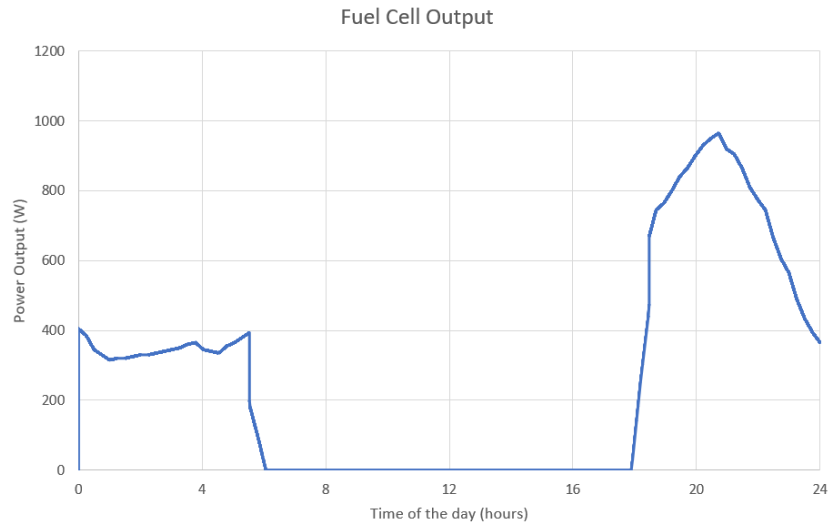


Figure 5.14 Power output of fuel cell under variable load conditions

Figure 5.15 illustrates the variation of the instantaneous net volume of hydrogen in standard litres under variable load conditions. The slope of the curve provides valuable insights into the operational dynamics of the system. A negative slope signifies fuel cell operation, indicating the consumption of hydrogen and a reduction in the volume of stored hydrogen. Conversely, a positive slope indicates electrolyzer operation, indicating the production of hydrogen and an increase in the volume of stored hydrogen.

At the beginning of the day, with no sunlight available, the net volume of hydrogen decreases as hydrogen is consumed by the fuel cell. However, around 6:30 am, the net volume starts to increase as the electrolyzer becomes operational, generating hydrogen from solar power. By the end of the day, the net volume of hydrogen reaches approximately 164 standard litres, indicating a net positive storage of hydrogen. This positive net storage implies that the energy produced by the solar array and subsequently converted into hydrogen by the electrolyzer surpasses the total energy consumed by the load throughout the day, including any heat losses. This observation highlights the effective energy management capabilities of the system, emphasizing its ability to efficiently store and utilize excess solar energy for sustained power generation.

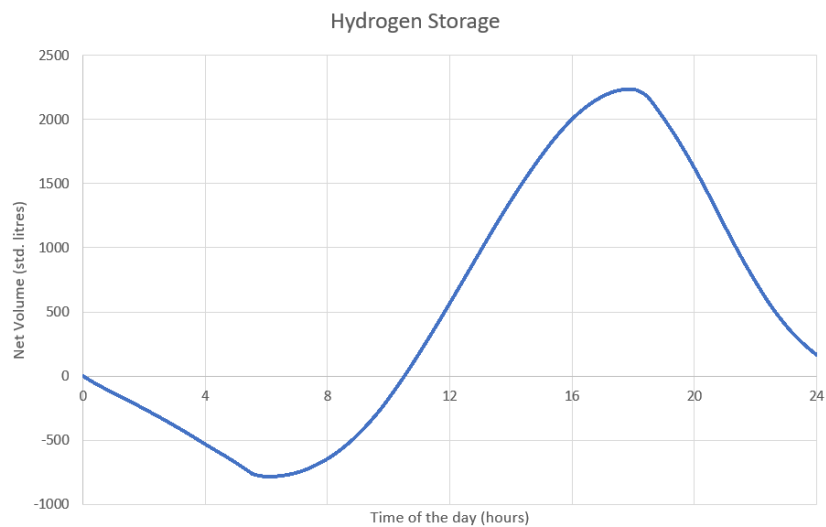


Figure 5.15 Net volume of hydrogen in hydrogen storage under variable load conditions

Figure 5.16 provides an insightful analysis of the efficiencies of the solar array, electrolyzer, and fuel cell under the variable load conditions. Notably, the efficiency of the solar PV array remains remarkably consistent throughout the operational period, ranging from 19.65% to 21.55%. On the other hand, the fuel cell efficiency exhibits some variation, with values ranging from 56% to 76% during operation. The efficiency of the electrolyzer demonstrates an intriguing pattern. The curve displays five distinct spikes on both sides of the afternoon timeframe. This phenomenon arises from the simulation's function, which adjusts the number of electrolyzers based on multiples of 400 W as the input power. Consequently, each time the input power of the electrolyzer reaches a multiple of 400 W, a spike appears in the curve, showcasing the impact of this adjustment. The efficiency of the electrolyzer fluctuates between 63.5% and 80% during operation. The observed variations underscore the intricacies involved in optimizing the efficiency of the electrolyzer and the fuel cell, which play a crucial role in the overall performance of the system.

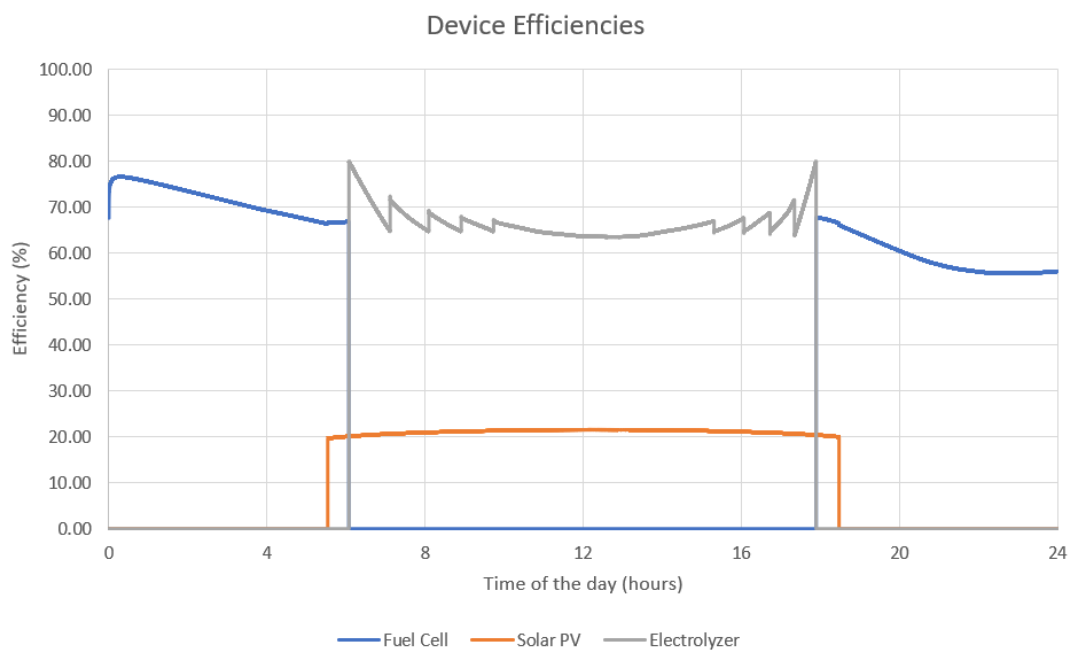


Figure 5.16 Variation of device efficiencies under variable load conditions

Figure 5.17 provides valuable insights into the operational heat generated by the electrolyzer and fuel cell. Both the electrolyzer and fuel cell exhibit operational heat curves that closely align with their respective outputs, suggesting a proportional relationship between the heat produced and the system output. The electrolyzer's operational heat reaches its peak at 817 W, while the fuel cell's operational heat peaks at 695 W. Similar to the observed spikes in the electrolyzer efficiency curve, the spikes in the electrolyzer's operational heat curve can be attributed to the same underlying reason mentioned previously. The cumulative heat production over the course of the day is calculated as 5.63 kWh for the electrolyzer and 3.77 kWh for the fuel cell, resulting in a total heat production of 9.4 kWh. Out of the total solar energy output of 19.61 kWh, 9.4 kWh is converted into heat due to inefficiencies in the system. The remaining 10.21 kWh is effectively utilized by the load and stored in the form of hydrogen, contributing to the overall energy efficiency of the system. These findings highlight the importance of considering and managing the heat generated by the electrolyzer and fuel cell, as it represents a significant portion of the system's energy losses.

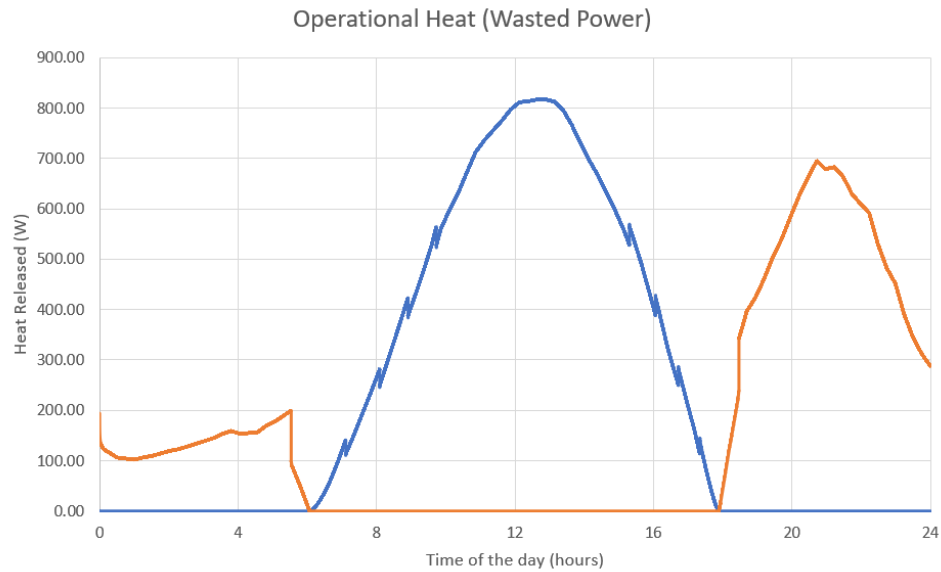


Figure 5.17 Operational heat produced by electrolyzer & fuel cell under variable load conditions

### 5.5.2 No Load

For no load scenario, the fuel cell never becomes operational and whatever power is output by the solar array goes straight into electrolyzer only.

Figure 5.18 showcases the electrolyzer output for the no load scenario. The electrolyzer operation begins when the solar array becomes operational, starting at around 5:45 am and ending around 6:15 pm. Notably, the electrolyzer output reaches its peak at 12 pm, when the solar power output is at its maximum. The curve follows the solar output curve exactly, being symmetrical about noon. The electrolyzer ceases operation in the absence of sunlight. The maximum observed molar flow rate of hydrogen reaches  $5.15 \times 10^{-3}$  mol/s.

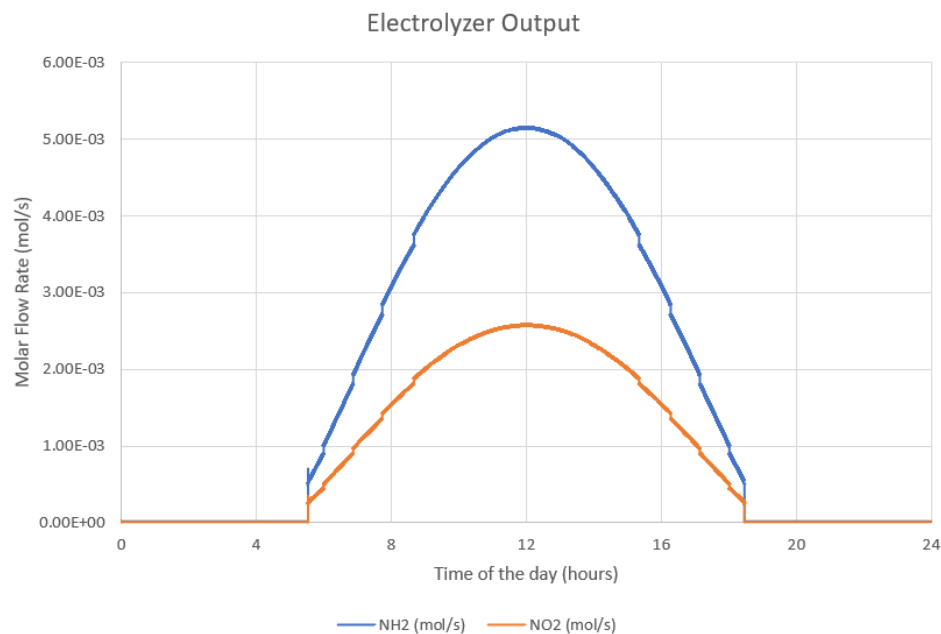


Figure 5.18 Gas molar flow rate output of electrolyzer under no load conditions

Figure 5.19 illustrates the instantaneous net volume of hydrogen in standard litres under no load conditions. The slope of the is always greater than or equal to zero, indicating the production of hydrogen and an increase in the volume of stored hydrogen during electrolyzer operation. At 5:45 am, the net volume starts to increase as the electrolyzer becomes operational, generating hydrogen from solar power. By the end of the day, the net volume of hydrogen reaches approximately 3645 standard litres.

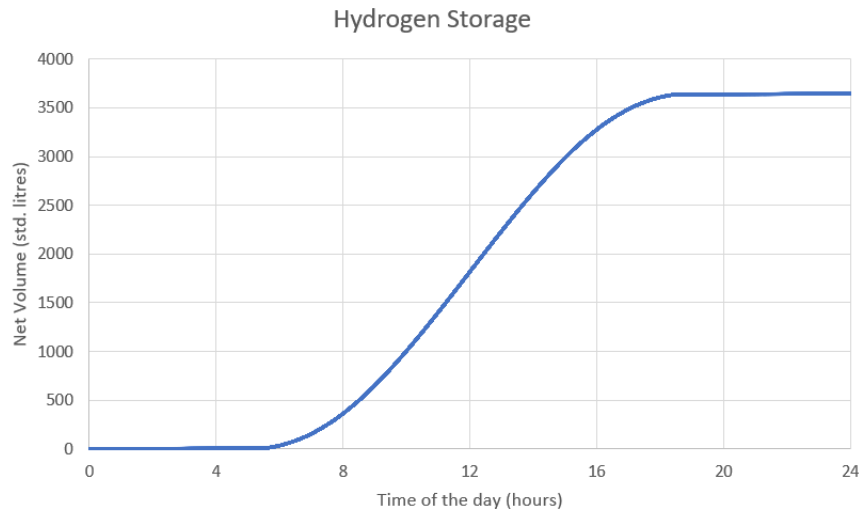


Figure 5.19 Net volume of hydrogen in hydrogen storage under no load conditions

Figure 5.20 shows the efficiencies of the solar array and electrolyzer under the no load conditions. The efficiency of the solar PV array is same as mentioned in variable load scenario. The efficiency of the electrolyzer demonstrates the same pattern exhibited in variable load. The efficiency of the electrolyzer fluctuates between 63.1% and 80% during operation.

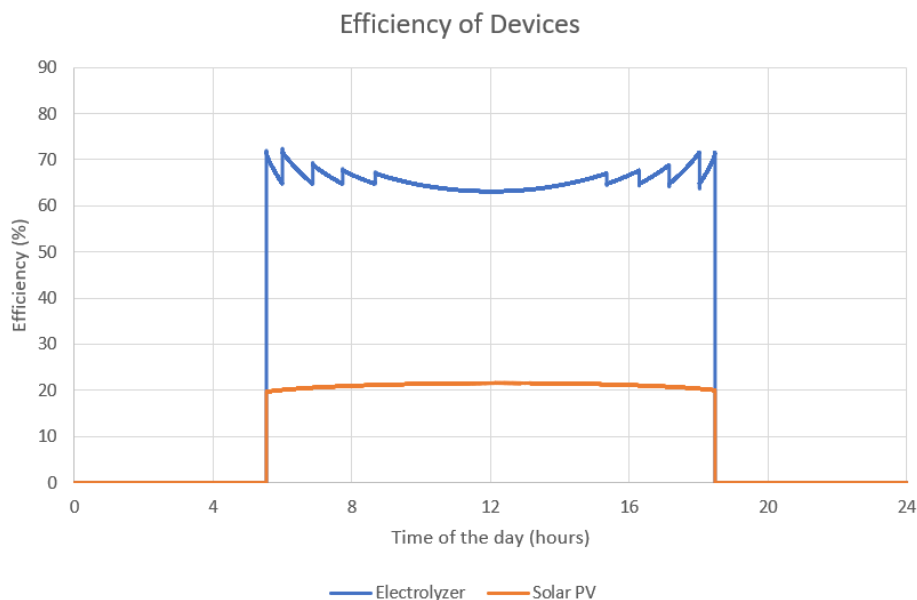


Figure 5.20 Variation of device efficiencies under no load conditions

Figure 5.21 shows the operational heat generated by the electrolyzer. The electrolyzer's operational heat reaches its peak at 861 W. The cumulative heat production over the course of the day is calculated as 6.86 kWh for the electrolyzer. Thus, out of the total solar energy output of 19.61 kWh, 12.75 kWh is effectively utilized by the load and stored in the form of hydrogen.

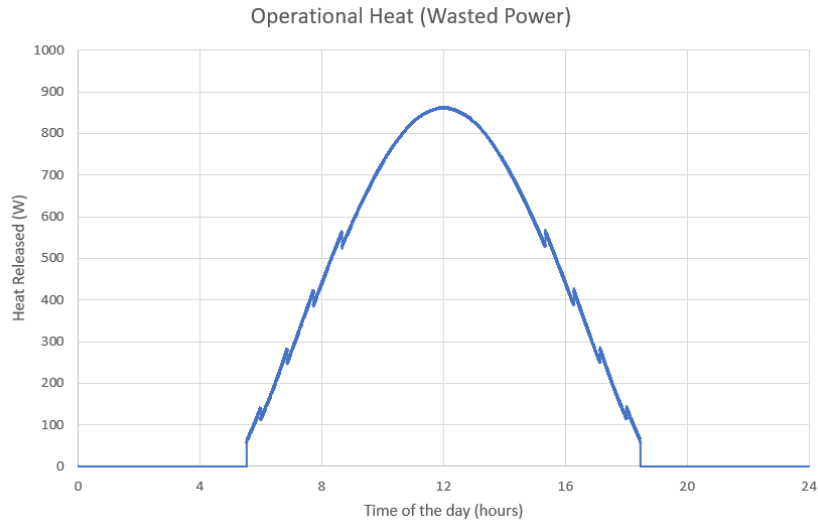


Figure 5.21 Operational heat produced by electrolyzer under no load conditions

### 5.5.3 Constant Load

The system is subjected to a constant load of 400 W throughout the day. The results obtained are expected to be similar to the results obtained in variable load, but with more symmetry.

Figure 5.22 showcases the electrolyzer output for the constant load scenario. The curve is symmetrical about noon, showing good performance of the model. The maximum observed molar flow rate of hydrogen reaches  $4.4 \times 10^{-3}$  mol/s.

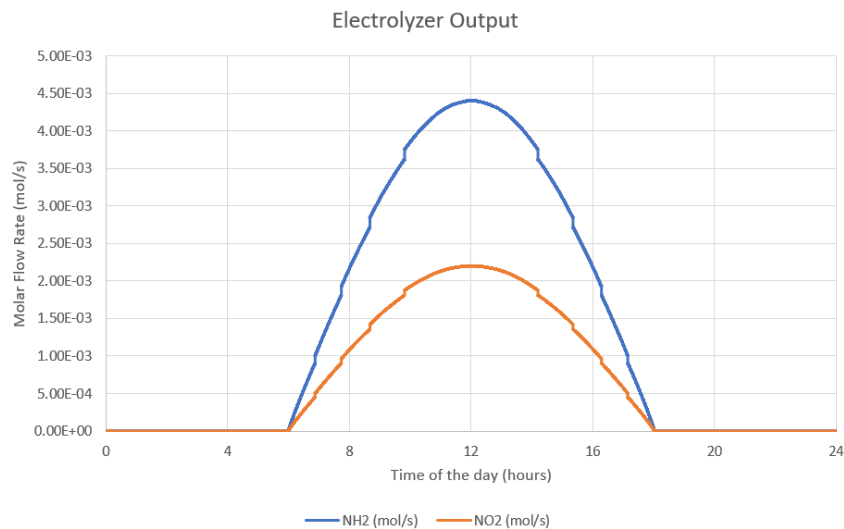


Figure 5.22 Gas molar flow rate output of electrolyzer under constant load conditions

Figure 5.23 illustrates the power output of the fuel cell for the constant load scenario. The power output of fuel cell is constant at 400 W matching the load.

Figure 5.24 illustrates the variation of the instantaneous net volume of hydrogen in standard litres under constant load conditions. By end of the day, the net volume of hydrogen reaches approximately 812 standard litres, indicating a net positive storage of hydrogen.



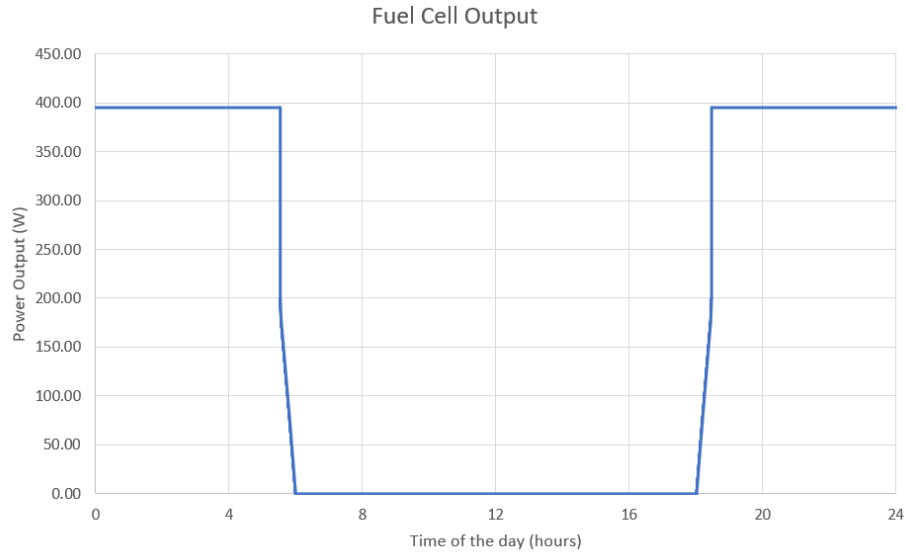


Figure 5.23 Power output of fuel cell under constant load conditions

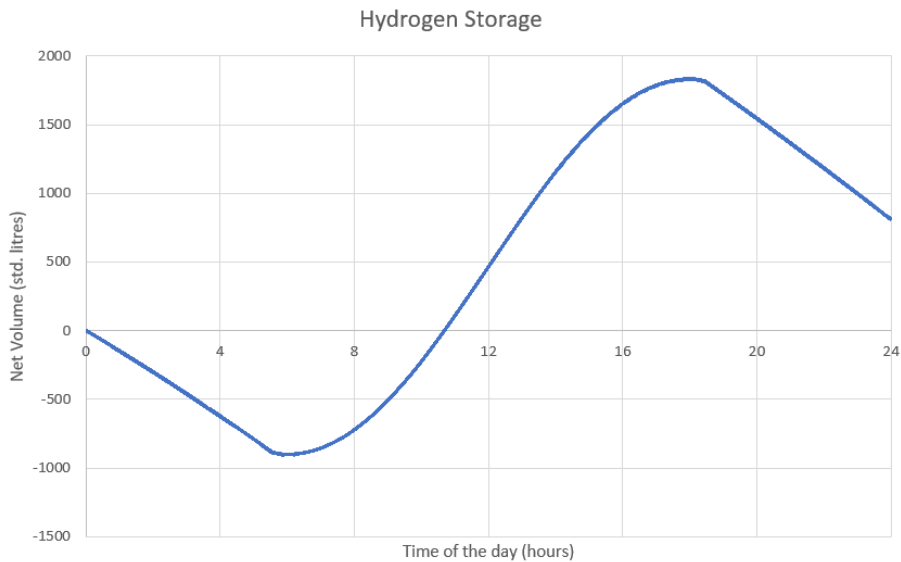


Figure 5.24 Net volume of hydrogen in hydrogen storage under constant load conditions

Figure 5.25 shows the efficiencies of the solar array, electrolyzer, and fuel cell under the constant load conditions. The efficiency of the solar PV array is same as in previous scenarios. Fuel cell efficiency exhibits variation from 56% to 76.6% during operation. The efficiency of the electrolyzer fluctuates between 63.7% and 80% during operation.

Figure 5.26 exhibits the operational heat generated by the electrolyzer and fuel cell. The electrolyzer's operational heat reaches its peak at 675 W, while the fuel cell's operational heat peaks at 264 W. The cumulative heat production over the course of the day is calculated as 4.91 kWh for the electrolyzer and 2.28 kWh for the fuel cell, resulting in a total heat production of 7.19 kWh. Out of the total solar energy output of 19.61 kWh, 12.42 kWh is effectively utilized by the load and stored in the form of hydrogen, contributing to the overall energy efficiency of the system.

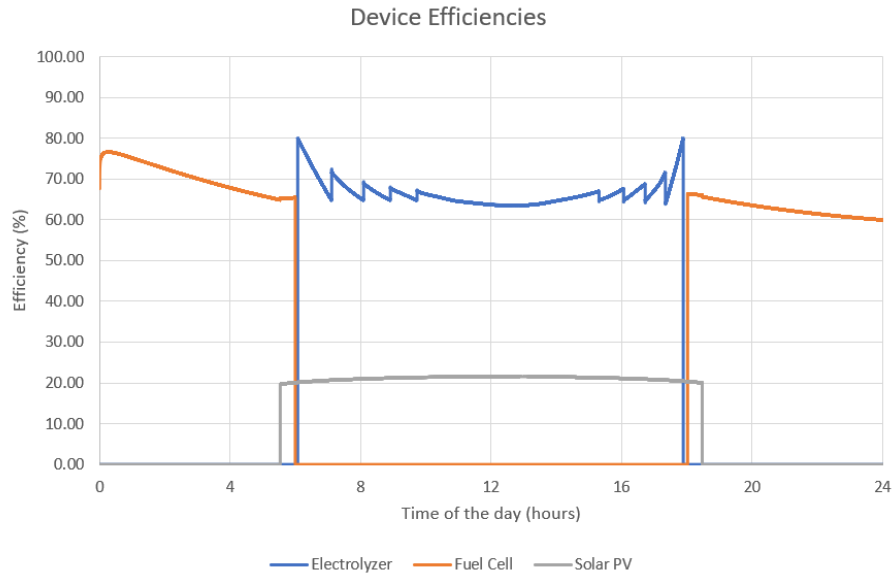


Figure 5.25 Variation of device efficiencies under constant load conditions

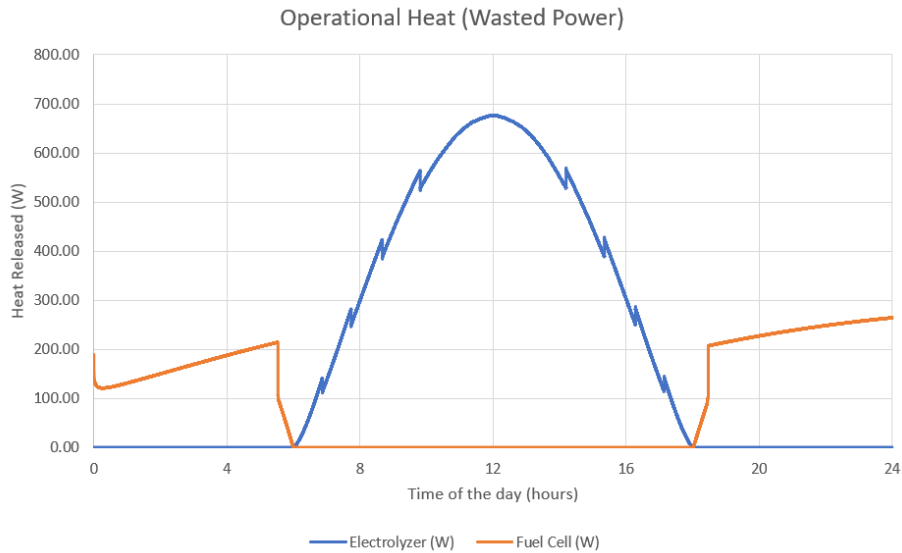


Figure 5.26 Operational heat produced by electrolyzer & fuel cell under constant load conditions

### 5.5.4 Comparison

The results obtained in the previous subsections validate the model for their respective operating conditions. A comparison of them can help get deeper insights into the functioning of the model.

Figure 5.27 presents a comparative analysis of the electrolyzer output for different load scenarios. Notably, the output of the no-load scenario surpasses or equals the output of the other two scenarios at every data point, affirming the viability of the developed model. Both the constant load and no-load curves exhibit a symmetrical pattern around noon. However, the curve corresponding to the variable load scenario displays a slight skew towards the right of noon. This skew is attributed to the specific nature of the load profile, which introduces variations in the electrolyzer output based on the changing load demands.

Furthermore, it is important to highlight that the starting and ending points of the no-load curve precede and succeed the corresponding starting and ending points of the other two scenarios, respectively. This observation indicates that the electrolyzer begins functioning earlier and ceases operation later in the absence of a load. These findings emphasize the responsiveness and adaptability of the electrolyzer to different load scenarios. Understanding these dynamics enables a better comprehension of the system's performance under various load conditions and aids in optimizing its operational efficiency.

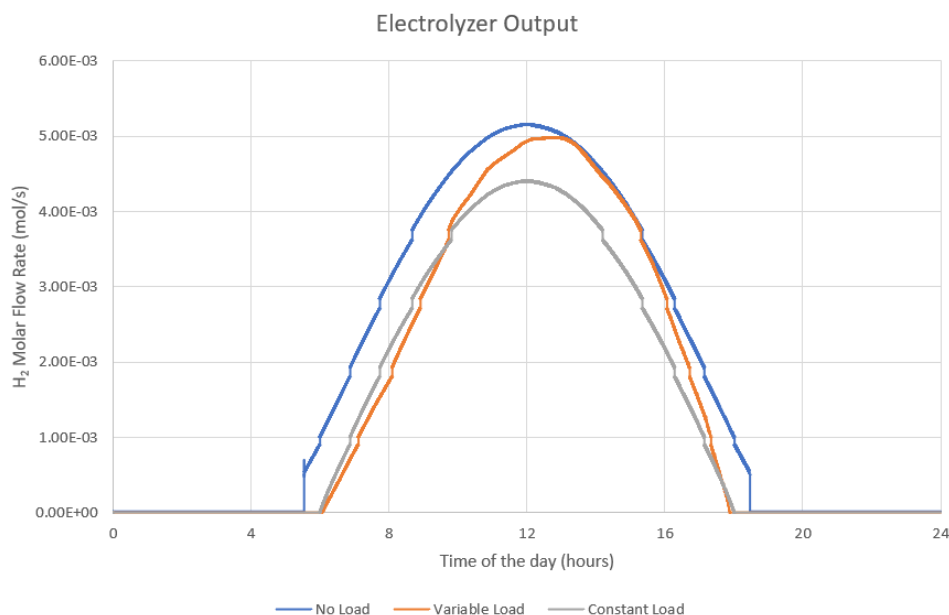


Figure 5.27 Comparison of gas molar flow rate output of electrolyzer under different loads

Figure 5.28 presents the dynamic changes in the instantaneous net volume of hydrogen in standard litres across different load scenarios. The net volume in the no-load scenario exhibits a continuous increase over time, reflecting a cumulative accumulation of hydrogen. In contrast, the net volume of the other two scenarios experiences fluctuations depending on whether the load surpasses the solar output or not. In the variable load scenario, the net volume curve intersects with the constant load curve at approximately 8 pm. This intersection occurs due to a sudden increase in the load demand within the variable load scenario, resulting in a steep decrease in the net volume. Conversely, the constant load curve changes relatively slowly throughout the operational period.

It is important to highlight that all three scenarios conclude with a net positive hydrogen volume, indicating an overall accumulation of hydrogen over time. Furthermore, the peak of the variable load curve surpasses that of the constant load curve. This arises from the interaction between the peak of the solar output and a minimum load demand within the variable load scenario, creating an optimal condition for hydrogen accumulation. In contrast, the constant load scenario does not exhibit the same synchronized dynamics between solar output and load demand.

These observations shed light on the variations in hydrogen volume under different load scenarios, providing valuable insights into the system's performance and the interplay between solar energy generation, load demand, and hydrogen storage. Understanding these dynamics enables informed decision-making for system optimization and load management strategies.

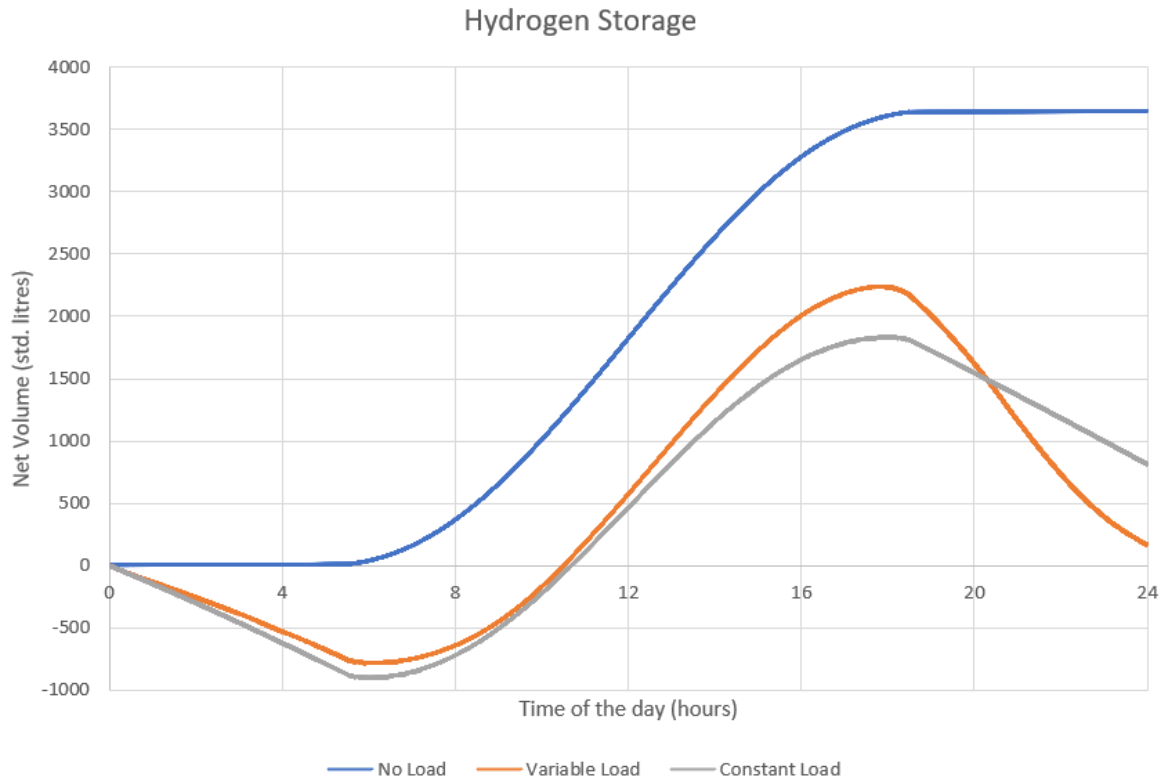


Figure 5.28 Comparison of net volume of hydrogen in hydrogen storage under different loads

In the context of passive solar system designs, it is generally observed that the efficiency of thermally insulated structures falls within the range of 50% to 70% [18]. For the purposes of the current project, an efficiency value of 60% has been chosen as the target benchmark. This selected value represents a reasonable and realistic efficiency goal for the project, taking into account the specific design considerations, insulation techniques, and energy utilization strategies implemented. By aiming for an efficiency level of 60%, the project acknowledges the importance of maximizing the utilization of solar energy and optimizing the overall thermal performance of the system. It is worth noting that achieving an efficiency of 60% requires a comprehensive approach encompassing various factors, such as insulation materials, glazing properties, solar orientation, and effective thermal management strategies. By aligning with this efficiency target, the project aims to contribute to the development of sustainable and energy-efficient passive solar system solutions.

The analysis of the energy generated by the solar array revealed that out of the total energy output of 19.61 kWh, the different load scenarios yielded varying amounts of heat. Specifically, the variable load scenario generated 9.4 kWh of heat, the no-load scenario produced 6.86 kWh, and the constant load scenario resulted in 7.19 kWh. These values indicate the thermal energy derived from the system in each respective case. Considering an assumed efficiency of 60% for utilizing this thermal energy to heat the interior space of the system, the overall system efficiencies were calculated for each scenario. The results indicate that the variable load scenario achieved an overall system efficiency of 80.8%, the no-load scenario demonstrated an efficiency of 86%, and the constant load scenario exhibited an efficiency of 85.3%.

These calculated efficiencies represent the effectiveness of the system in utilizing the generated solar energy to power the load and for heating purposes, accounting for the specific load scenarios. The variations in efficiency among the different scenarios highlight the impact of load demand on the overall system performance.

These findings underscore the importance of optimizing the load management strategies and system design to maximize the utilization of solar energy and enhance the overall efficiency of the system. By continuously assessing and improving the system's efficiency, it is possible to advance the development of sustainable energy solutions and promote the effective utilization of renewable resources in practical applications.

## 6. Conclusion

This report has presented a comprehensive analysis of a solar-powered hydrogen generation and storage system, investigating its performance under different load scenarios. Through detailed modelling and simulation, the study has provided valuable insights into the system's dynamics and its ability to harness solar energy, produce hydrogen, and store it efficiently.

The results have demonstrated the system's adaptability and responsiveness to varying load demands. The variable load scenario showcased the system's capability to adjust its operation according to changing power requirements, optimizing hydrogen production and storage. The no-load scenario revealed the system's potential for hydrogen accumulation and storage, ensuring a net positive volume over time. Furthermore, the comparison of the constant load scenario with other scenarios has highlighted the importance of load management strategies in maximizing system efficiency. The findings underscore the need for optimizing load profiles to match solar output and enhance overall system performance.

Overall, the solar-powered hydrogen generation and storage system presents a promising solution to address the intermittency of solar energy and contribute to a sustainable energy future. By effectively harnessing solar power, generating hydrogen, and optimizing load management, the system offers a pathway towards a cleaner and more resilient energy system.

The round-trip efficiency of electricity to hydrogen to electricity via electrolyzer-fuel cell path is generally around 35-50 %. But utilising the heat produced and not letting it get lost to the surroundings increases the effective efficiency to above 80-90 %. This makes the current solar hydrogen system viable.

With the help of this project, soldiers can get the following benefits:

- i. **Electricity:** useful for electrolyzer and general purposes
- ii. **Hydrogen:** useful to generate electricity when the solar power supply is not possible. Also, exploring other benefits of hydrogen like hydrogen therapy and hydrogen fuel
- iii. **Oxygen:** useful for medical purposes and health-related issues
- iv. **Heat:** can warm themselves up when conditions outside are highly unfavourable or can comfort themselves for a brief period

Moving forward, further research and development are essential to refine the system design, improve component efficiency, and explore integration with other renewable energy technologies. Continued advancements in solar-powered hydrogen systems will accelerate the transition to a low-carbon future and promote the widespread adoption of renewable energy sources.

In conclusion, the findings of this study provide valuable insights into the performance and potential of solar-powered hydrogen systems. The study underscores the significance of efficient load management, highlighting the need for continued research and optimization. By advancing these systems, we can contribute to a sustainable and cleaner energy future, driving the global energy transition towards a more resilient and environmentally friendly path.

## References

- [1] Privitera, S.M.S., M. Muller, W. Zwaygardt, M. Carmo, R.G. Milazzo, P. Zani, M. Leonardi, F. Maita, A. Canino, M. Foti, F. Bizzarri, C. Gerardi, and S.A. Lombardo. 2020. "Highly efficient solar hydrogen production through the use of bifacial photovoltaics and membrane electrolysis." *Journal of Power Sources* 473:228619.
- [2] Liu, Guanyu, Yuan Sheng, Joel W. Ager, Markus Kraft, and Rong Xu. 2019. "Research advances towards large-scale solar hydrogen production from water." *EnergyChem* 1(2):100014.
- [3] Joshi, Anand S., Ibrahim Dincer, and Bale V. Reddy. 2011. "Solar hydrogen production: A comparative performance assessment." *International Journal of Hydrogen Energy* 36(17):11245-11257.
- [4] Wang, Hongsheng, Hui Kong, Zhigang Pu, Yao Li, and Xuejiao Hu. 2020. "Feasibility of high efficient solar hydrogen generation system integrating photovoltaic cell/photon-enhanced thermionic emission and high-temperature electrolysis cell." *Energy Conversion and Management* 210:112699.
- [5] Jonas, James. 2009. "THE HISTORY OF HYDROGEN." *AltEnergyMag*, April 1. Retrieved July 20, 2022 (<https://www.altenergymag.com/article/2009/04/the-history-of-hydrogen/555/>).
- [6] Yilanci, A., I. Dincer, and H.K. Ozturk. 2009. "A review on solar-hydrogen or fuel cell hybrid energy systems for stationary applications." *Progress in Energy and Combustion Science* 35(3):231-244.
- [7] Shabani, Bahman., John Andrews. 2011. "An experimental investigation of a PEM fuel cell to supply both heat and power in a solar-hydrogen RAPS system." *International Journal of Hydrogen Energy* 36(9):5442-5452.
- [8] Jafari, Moharm., Davoud Armaghan, S.M. Seyed Mahmoudi, and Ata Chitsaz. 2019. "Thermoeconomic analysis of a standalone solar hydrogen system with hybrid energy storage." *International Journal of Hydrogen Energy* 44(36):19614-19627.
- [9] Krismadinata, Nasrudin Abd. Rahim, Hew Wooi Ping, and Jeyraj Selvaraj. 2013. "Photovoltaic module modeling using simulink matlab." *Procedia Environmental Sciences* 17:537-546.
- [10] Goswami, D. Yogi. 2015. *Principles of Solar Engineering*. 3rd ed. Boca Raton: CRC Press.
- [11] Cockerill, Rob. "Electrolyzer technologies PEM vs Alkaline electrolysis." *Nel Hydrogen*, Retrieved October 10, 2022 (<https://nelhydrogen.com/resources/electrolyzer-technologies-pem-vs-alkaline-electrolysis/>).
- [12] University of Cambridge. "Types of Fuel Cells." Retrieved October 11, 2022 (<https://www.ceb.cam.ac.uk/research/groups/rg-eme/Edu/fuelcells/types-of-fuel-cells>).
- [13] Wangchuk, Sonam. 2021. "The LADAKH Tent | World's 1st Solar Heated Military Tent | Made in India | Sonam Wangchuk." YouTube video, 13:03. ([https://www.youtube.com/watch?v=IF-IYkU0gmQ&ab\\_channel=SonamWangchuk](https://www.youtube.com/watch?v=IF-IYkU0gmQ&ab_channel=SonamWangchuk)).



- [14] Abdin, D., C.J. Webb, and E. MacA. Gray. 2015. "Modelling and simulation of a proton exchange membrane (PEM) electrolyser cell." *International Journal of Hydrogen Energy* 40(39):13243-13257.
- [15] Khan, M.J, M.T. Iqbal. 2005. "Modelling and Analysis of Electro-chemical, Thermal, and Reactant Flow Dynamics for a PEM Fuel Cell System." *Fuel Cells* 5:463-475.
- [16] Weather Spark. "Climate and Average Weather Year Round in Leh India." Retrieved April 7, 2023  
(<https://weatherspark.com/y/109277/Average-Weather-in-Leh-India-Year-Round#Sections-Temperature>).
- [17] NREL. "NSRDB: National Solar Radiation Database." Retrieved May 11, 2023  
(<https://nsrdb.nrel.gov/data-viewer>).
- [18] Kumar, Amit. 2014. "Solar Energy for Passive House Design." *International Journal of Engineering Research & Technology* 3(1):955-966.
- [19] Bernardi, Dawn M., and Mark W. Verbugge. 1991. "Mathematical Model of a Gas Diffusion Electrode Bonded to a Polymer Electrolyte." *AIChE Journal* 37(8):1151-1163.
- [20] Gou, Bei, Woon Ki Na, and Bill Diong. 2010. *Fuel Cells: Modeling, Control, and Applications*. Boca Raton: CRC Press.